Powder Technology 438 (2024) 119591

Contents lists available at ScienceDirect

Powder Technology

journal homepage: www.journals.elsevier.com/powder-technology

Method for Material Extrusion Additive Manufacturing process made of bio-based polymer. Application for tool steel powders

N. Charpentier [a,b], T. Barrière [a,*], F. Bernard [b], N. Boudeau [c], A. Gilbin [c], P. Vikner [d]

[a] Université de Franche-Comté, CNRS, institut FEMTO-ST, Département Mécanique Appliquée, 24 chemin de l'Epitaphe, 25000 Besançon, France
[b] Laboratoire Interdisciplinaire Carnot de Bourgogne - UMR 6303 CNRS/Université Bourgogne Franche-Comté, 9, Avenue Alain Savary BP 47870, Cedex, Dijon 21078, France
[c] SUPMICROTECH, CNRS, institut FEMTO-ST, Département Mécanique Appliquée, 24 chemin de l'Epitaphe, 25000 Besançon, France
[d] Aubert & Duval, Aubert & Duval, Rue du Villa, 63770 Les Ancizes, France

HIGHLIGHTS

- Development of bio-based feedstock pellets for Material Extrusion.
- Influence of binder composition and metallic powder size on the process.
- Influence and control of the porosity along the whole process.
- Low porosity and flawless net shape parts with optimised post-treatment stages.

GRAPHICAL ABSTRACT

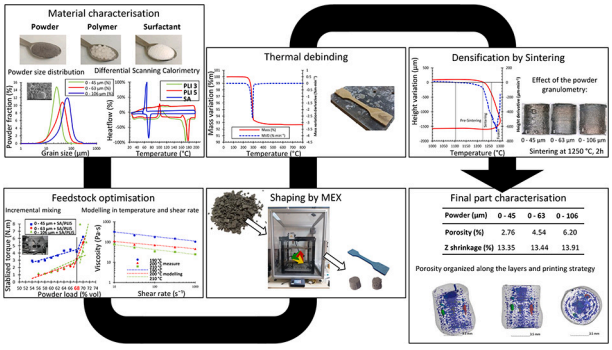

ARTICLE INFO

Keywords:
Material Extrusion Additive Manufacturing
Bio-based feedstock
PolyLactic acid
Tool steel powder
Fused granulate fabrication

ABSTRACT

The aim of the paper is to propose the development of a MEX feedstock composed of a bio-sourced binder and a tool steel powder to be printed with a pellet printer.

A bio-based feedstock with the highest powder load is made using different powder sizes. It is shaped into test samples with Fused Granulate Fabrication process, from where the polymer binder is then eliminated by thermal degradation. The resulting powder skeleton is densified by conventional sintering, to achieve a maximal density. The densified samples are examined by X-ray tomography for the evaluation of their internal porosity. The developed method permits to get, from optimised stages, final components with a high density of 97%, equivalent to that obtained using conventional PIM processes, with a dimensional shrinkage of 13%. The physico-chemical composition of the densified components obtained is in line with the literature.

* Corresponding author.
E-mail address: thierry.barriere@univ-fcomte.fr (T. Barrière).

https://doi.org/10.1016/j.powtec.2024.119591
Received 19 April 2023; Received in revised form 22 January 2024; Accepted 3 March 2024
Available online 5 March 2024

Glossary

3 D	Three-dimensional
3 DP	3 D Printing
ABS	Acrylonitrile Butadiene Styrene
AM	Additive Manufacturing
BET	Brunauer–Emmett–Teller
CAD	Computer-Aided Design
DBP	DiButyl Phtalate
DOE	Design Of Experiments
DSC	Differential Scanning Calorimetry
EVA	Ethylene-Vinyl Acetate copolymer
FFF	Fused Filament Fabrication
FTP	Failure to print
HIP	Hot Isostatic Pressing
MEX	Material Extrusion
MFI	Melt Flow Index
MVD	Mass Variation Derivative
PA	Palmitic Acid
PE	PolyEthylene
PEG	PE Glycol
PHBV	Poly(3-HydroxyButyrate-*co*-3-HydroxyValerate)
PIM	Powder Injection Moulding
PLA	PolyLactic Acid
PMMA	PolyMethyl MethAcrylate
PP	PolyPropylene
PPC	PolyPropylene Carbonate
PSD	Particle Size Distribution
PW	Paraffin Wax
SA	Stearic Acid
scCO2	supercritical CO2
SEM	Scanning Electron Microscope
SS	Stainless Steel
TGA	ThermoGravimetric Analysis

Notation

Ss	Specific surface m^2/g
Cu	Coefficient of uniformity
Fag	Agglomeration factor
S_w	Distribution slope parameter
μ	Viscosity in Pa·s
$\dot{\gamma}$	Shear rate in s^{-1}
K	Consistency index of the Power law in $Pa{\cdot}s^2$
n	Flow behaviour index of the Power law
T	Temperature in Kelvin
B	Factor of the Arrhenius law in $Pa{\cdot}s^2$
E_a	Activation energy in $J{\cdot}mol^{-1}$
R	Constant of perfect gasses in $J{\cdot}mol^{-1}{\cdot}K^{-1}$
Tg	Glass transition temperature in K
Tc	Crystallization temperature in K
Tm	Melting temperature in K
R^2	Coefficient of determination
Sc	Surfactant concentration in $mg{\cdot}m^{-2}$

1. Introduction

In the past decade, 3D Printing (3 DP) has experienced a rising popularity, both for industrial and domestic use. Its ease of use, adaptability and relative low cost make it the main method for prototyping. But 3 DP is limited by the primary material. Usually, polymer filaments are used because their fusion temperature is relatively low (200 to 250 °C) and polymers are not brittle. In the 2000 s, where 3 DP was protected with patents, researchers have experimented the use of new primary materials, to get final parts with better functional characteristics. Among these new materials, Powder Injection Moulding (PIM)-like feedstocks have been explored, where a polymer is used as binder to shape components from piezoelectric materials for example [1].

In the 70s, similar developments had been led in the field of polymer injection where polymers loaded with ceramic or metallic powders were employed as a vector for shaping ceramic or metallic parts with injection moulding press. This advanced process known as PIM has proved its industrial viability and is nowadays largely used for mass production of complex metallic or ceramic components. A detailed presentation of the PIM processes is done in [2], while [3] presents the application of PIM for manufacturing medical ceramic-based components.

The PIM-like Material Extrusion (MEX) is a process, which uses feedstock like the PIM process, but where components are shaped with 3DP process; the shaping step must be followed by debinding and sintering stages to obtain, like for PIM, dense parts. This allows the fabrication of quite functional parts with low-cost machines; the main drawback is the resulting important surface roughness. MEX process is more attractive in terms of design freedom; moreover, it does not require a metal mould compare to PIM process. As part of the work carried out by S.I. Roshchupkin in [4], an extruder is specially designed for the manufacture of metal-polymer filament for additive technologies, where the filament can be wound directly at the extruder outlet, even for highly powdered mixtures. In addition, the analyses of C. Suwanpreecha in [5] concluded that this process can manufacture end-use metallic components. According to their study, there are still major gaps to be filled at every stage of the MEX process. Many aspects, such as homogeneity, mechanical properties, geometrical precision and production rates, still need to be improved. Despite technological advances, it still needs further work to fine-tune the process or to produce a filament with the right extrusion properties.

Moreover, MEX process allows the use of a wide range of materials. Other Additive Manufacturing techniques based on powder bed (such as Selective Laser Melting or Electron Beam Melting), or the Direct Energy Deposition processes, can shape metals, but they need the use of an adapted binder for shaping ceramics as it is described by Wang et al. in [6]. MEX can be used with PIM-like feedstock, but also with other extruded materials. MEX regroups processes such as robocasting [7] or binder-deposition [8], where the part is shaped using a carrier fluid, followed by additional steps for its densification. Rane and Strano describe extensively the different MEX processes in [9] and start an inventory of the different studied feedstock and powders, while in [10] an extensive review of MEX applied for metals is proposed. In [11], Gonzalez et al. focus on MEX methods for metals and ceramics. In the work of Vetter et al. in [12], the development of a material extrusion process for a tool steel involving Fused Filament Fabrication (FFF) printing is carried out and leads to 3 D-shaped components with excellent mechanical properties. The work carried out by Lu et al. in [13] concerns the development of an FFF printing process based on a binder formulation based on PLA charged with bronze powders. Their control of the technological developments permits them to get oxidation-free microstructures for the printed components; moreover, the resulting mechanical properties were very satisfying. In addition, MEX sintered parts can present a higher density, as a controlled conventional sintering generally creates shrinkage in the part when removing voids.

In recent years, MEX has stimulated a great research interest using available PIM feedstock or producing new blends adapted for this process, where the binders generally use derivatives from the PIM industry, with a high prevalence of oil-based polymers. Traditional formulations use PolyPropylene (PP) [14], PolyEthylene (PE) or PE Glycol (PEG) [15] and Paraffin Wax (PW), which are all synthetized from petroleum

products. Recent developments in polymer research make possible the synthesis of petroleum-free PE [16], but the commercial Bio-PE unfortunately tends to include some petroleum-based PE. FFF is already well optimised to be used with PolyLactic Acid (PLA) which is a biobased polymer already used in PIM processes, with PEG [17] or with Poly-Methyl MethAcrylate (PMMA) [18]. Feedstocks based on PLA for industrial application are not currently available, and they are not so much used in academic research, whereas it would be a way to reduce the ecological footprint of such processes.

Powder plays only a weak role during the printing step, as its characteristics are revealed during the densification stage. During the printing stage, only the granulometry is important as it influences the maximal volume loading and then, the resulting shear viscosity behaviour of the feedstock.

Apart from being printable, the other optimised parameter is the porosity of the final part. Porosity presents an important influence on the mechanical characteristics of the resulting structural material; thus, it is a limiting parameter for the MEX process.

Based on the results of Clemens et al. in [19], it is recommended to investigate the quality of the filament, with rheological studies, before printing ceramic components; in their work, the flow study permits to adjust printing parameters, to avoid printing problems like filament buckling or abrasion. To avoid the need of a calibrated filament, a Fused Granular Fabrication (FGF) printing process is chosen. Wick-Joliat et al. in [20] lead works on FGF printing process coupled with debinding and sintering steps, where pellets based on thermoplastic binder with a high quantity of ceramic powder are used; they were able to manufacture heat-temperature element components composed of an electrical conductive and a non-conductive support structure. In Lieberwirth et al.,'s preliminary study in [21], the quality of green printed samples produced by the FGF process with a specially developed extruder is similar to the ones obtained with the typical FFF process, in terms of shape and shrinkage after the final sintering process for metal powders. Their results open up the possibility of exploiting a large variety of powders and higher particle sizes. In this case, 3D printing based on the extrusion of pellets is selected. Singh et al. in [22] [23] studied the MEX printing process with FGF for copper powders using PolyMIM pellets. They obtained fully dense copper components after optimizing the kinetics for debinding and the sintering parameters.

FGF 3D printing technology using a feedstock, which is directly inserted into the print head, represents a cost-saving solution. This is this technological solution, which is chosen in the present study, where a specific pellet print extruder for highly powder-filled materials is implemented. The aim of the paper is to propose the development of a Material Extrusion feedstock composed of a bio-sourced binder and a tool steel powder to be printed with a pellet printer. In addition, the influence of powder granulometry on the overall process is also analysed. The final composition and properties of densified printed components is also studied. In the first part, the method to design an original feedstock suitable for the MEX process is described. To do that, different polymer grades and various powder sizes are studied. The choice of the powder and of the binder components is described, along their respective characterisations. In a second part, the created feedstocks are modelled as rheological behaviour law and the optimal parameters of printing are chosen by conducting a Design of Experiment. Debinded samples and final sintered components are characterized in order to study the shrinkage, porosity, roughness, microstructure, and to quantify the influence of the powder size on the final porosity and the geometrical shrinkage.

2. Methods and materials

2.1. Powder characterization

The powders used in this study are ASP2023 steel-tool alloy powders. They are produced by gas atomization and supplied by Auber & Duval company [24]. The atomised powders are sieved with different meshes resulting in different powders named by the mesh size. For example, the powder named 0–60 μm corresponds to a powder material sieved with a 60 μm mesh screen.

Powders are characterized with a Particle Size Distribution (PSD) usually described in percentiles named d_x; if $d_x = y$, it means that x % of the particles of powder is finer than y μm. There is its counterpart in volume, written dv_x, which measures with the same method, the percentile in volume. For the present powders, four parameters are used: d_{10}, d_{50}, d_{60} and d_{90}, which permit to evaluate other powder characteristics such as those presented in the following.

The Specific Surface (Ss) of a powder corresponds to its real surface area. Two grains may have the same size but very different Specific Surfaces, depending if their surface is smooth or coarse. A powder having a large Specific Surface is very reactive; so, powders with very different Ss present very different behaviours. The Specific Surface of a powder can be measured with a Krypton retention test where gas adsorption is measured when the powder is submerged in Krypton gas [25]. The Krypton is naturally adsorbed at the surface, is stabilized by reducing the sample temperature and the excess gas is then vacuumed. The remaining Krypton adsorbed at the surface is released by increasing the temperature; the quantity of remaining gas is used to evaluate the Specific Surface by using the Brunauer - Emmett - Teller (BET) Eq. [25]. This test is done in a Micromeritics Specific Surface Analyser.

The coefficient of uniformity, noted *Cu*, characterizes whether the powder distribution is uniform (if $Cu < 6$) or not (if $Cu > 6$). *Cu* is calculated with the following equation:

$$Cu = \frac{d_{60}}{d_{10}} \tag{1}$$

Another important powder parameter is the Agglomeration factor written *Fag*. It represents the size of the agglomerate in the powder against the mean size of the single particles. When a powder does not contain agglomerate, its *Fag* parameter tends to 1. It is calculated with the Eq. (2):

$$Fag = \frac{dv_{50}}{d_{BET}} \tag{2}$$

where dv_{50} is the cumulative percentile size at 50% by volume of the powder, and d_{BET} the average diameter from the specific area measurement. d_{BET} is calculated with Eq. (3):

$$d_{BET} = \frac{6}{\rho \bullet Ss} \tag{3}$$

where ρ is the density of the material, measured with a Micromeritics AccuPyc Pycnometer.

The distribution slope parameter noted S_w, is the last significant characteristic, used to quantify the flow behaviour of the powder in a feedstock. S_w is calculated with Eq. (4) below:

$$S_w = \frac{2.56}{log\left(\frac{d_{90}}{d_{10}}\right)} \tag{4}$$

A distribution slope parameter S_w below 2 indicates that the powder has a large distribution, and will have a fluid flow inside the feedstock. A $S_w > 4$ indicates that the powder has a reduced distribution; its flow would be more viscous and could cause issues when used in a feedstock.

Finally, SEM analysis with ASTM E2142–08 standard is used to observe powder shape details.

2.2. Feedstock development

The feedstock development for MEX follows the same method than for PIM. It consists in optimizing the feedstock parameters such as the specific shear rate (from 100 to 1000 s^{-1}) and the proportion of powder;

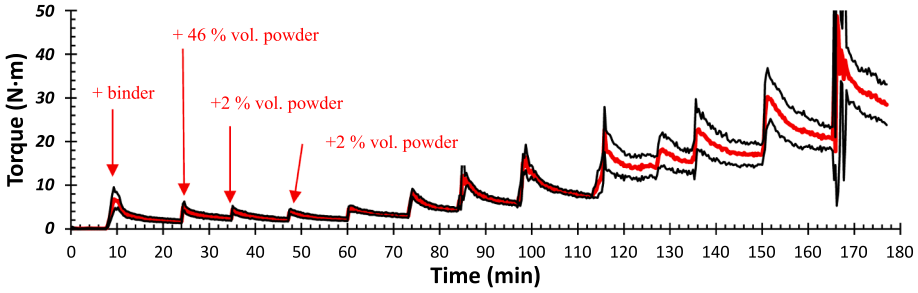

Fig. 1. Incremental mixing of a PP/PEG/SA + $MoSi_2$ feedstock starting at 46%vol. at 180 °C with 30 rpm. In red the mean torque, in black the min and max torque.

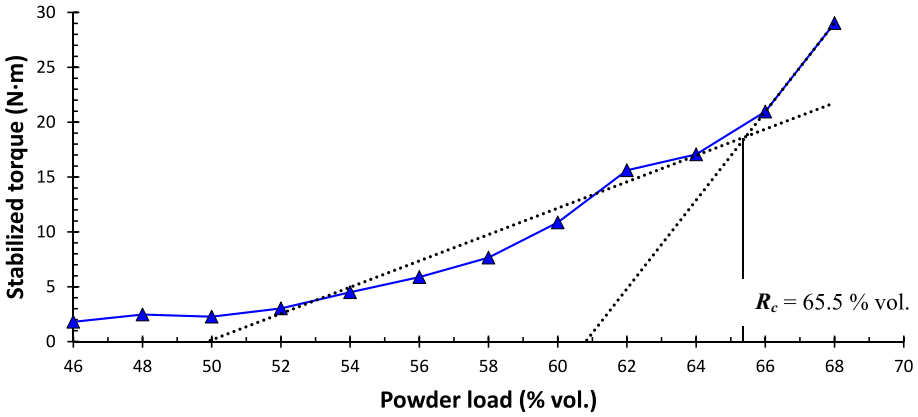

Fig. 2. Analysis curve of the incremental mixing of Fig. 1.

Table 1
: Different feedstock materials, their respective debinding methods and kinetic time cycles.

Binder system				Powder	Debinding procedure			Total	Ref
Primary binder	Backbone binder	Surfactant	Other		Solvent	$scCO_2$	Thermal		
PW	PP	SA	–	Al_2O_3			X	40 h	[36]
			Carnauba Wax	MIM-4605	X		X	18 h	[37]
			DBP	ZrO_2	X		X	19 h	[38]
	PE	SA	–	Al_2O_3			X	17.9 h	[39]
					X		X	13.7 h	
				Al_2O_3, ZrO_2	X		X	27.2 h	[40]
				NdFeB	X		X	15 h	[41]
								68.3 h	[42]
								36 h	[43]
			DBP	ZrO_2	X		X	19 h	[38]
	PE + EVA	SA	–	NdFeB	X		X	15 h	[41]
	EVA	SA	–	Al_2O_3			X	150 h	[44]
			DBP	ZrO_2	X		X	19 h	[38]
PEG	PP	SA	–	IN718	X		X	52.5 h	[17]
						X	X	7.5 h	[45]
	PMMA	SA	–	IN718	X		X	18.6 h	[46]
	PMMA + PPC	SA	–	CP-Ti	X		X	21 h	[47]
	PLA	SA	–	IN718	X		X	52 h	[17]
						X	X	7.2 h	[45]
	PHBV	SA	–	IN718		X	X	6.8 h	[45]
	PolyMIM	PolyMIM	PolyMIM	SS17–4 PH	X		X	23 h	[15]

that last one should be as large as possible to minimise the porosity and, consequently the shrinkage which can occur during the subsequent debinding and sintering stages.

The powder loading rate is determined by the incremental mixing method, which is described in [26] [27] along other critical loading identification tests. It presents the advantage of rapidity by using a twin-screw mixer Plastograph EC W50EHT, composed of two counter-rotating screws in a thermo-regulated mixing chamber of 50 cm^3. The test is conducted by mixing the selected polymer binder at a specific temperature of 190 °C and a specific turning speed, in which a powder is

Table 2
: Polymer and Surfactant characteristics from supplier Natureplast.

Material	Name	Type	Density	MFI (g / 10 min.) at 190 °C	*Tm* (°C)	D-isomer (%)
PLA	PLI 3	Amorphous	1.24	35	185	1.5
PLA	PLI 5	PLLA	1.25	25–35	170–180	0.5
PLA	PLE 5	PLLA	1.25	7	170–180	0.2
PLA	PLE 5-A	Amorphous	1.24	3	155	3.4
SA	N/A	N/A	0.845		68–70	na

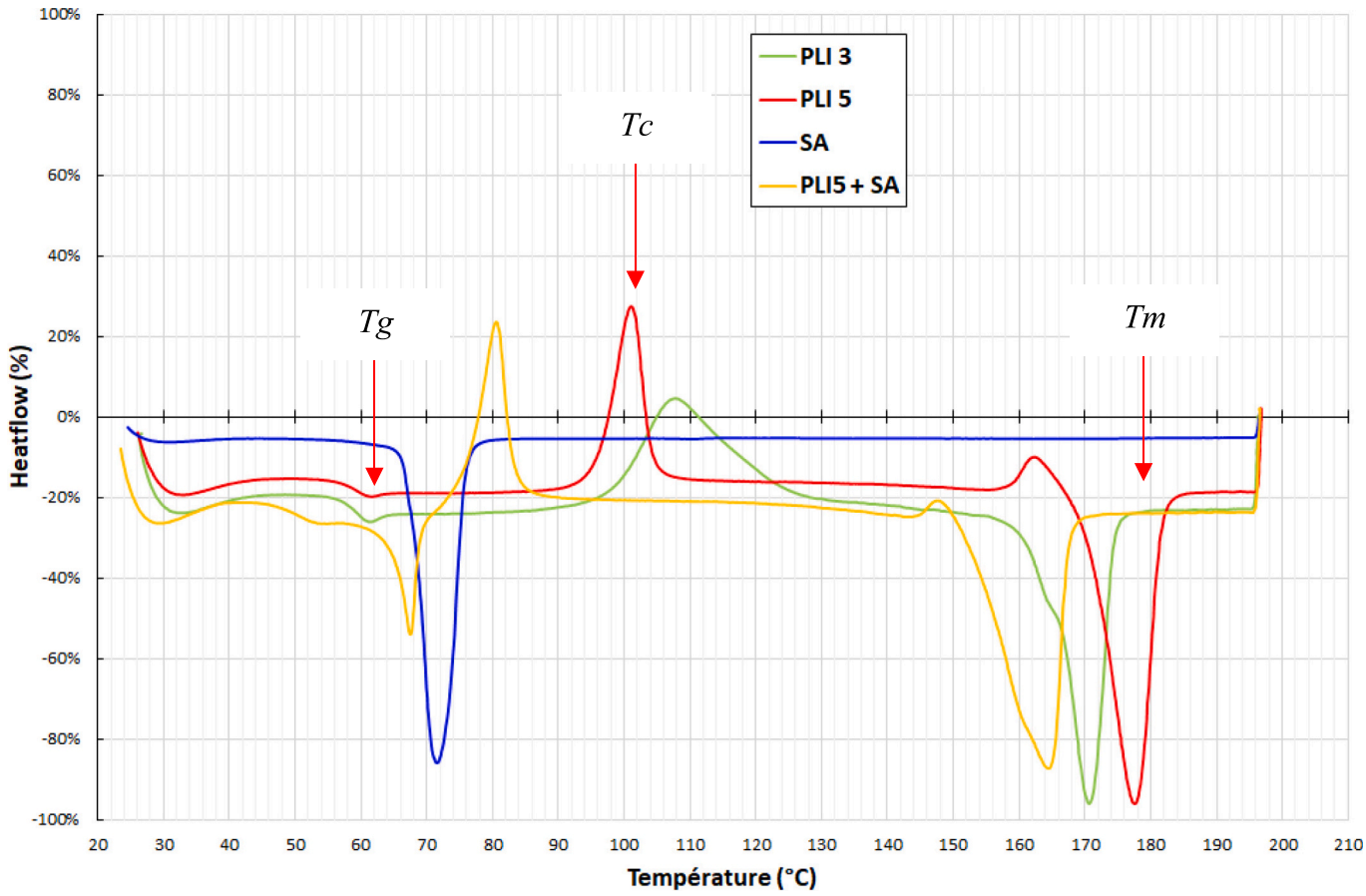

Fig. 3. DSC analysis of the binder components.

Table 3
Measured Polymer and Surfactant characteristics by DSC.

Name	Type	*Tg* (°C)	*Tc* (°C)	*Tm* (°C)
PLI3	Amorphous	62 ± 1	110 ± 1	171 ± 1
PLI5	PLLA	62 ± 1	108 ± 1	178 ± 1
SA	na			72 ± 1

gradually added. The torque needed for the screw to turn at 30 rpm is continuously measured. A screw speed of 30 rpm is an optimal value during mixing process with the twin screw mixer for MIM pellets elaboration in order to obtain homogeneous feedstock without segregation defects [28]. An example of an incremental mixing method is presented in Fig. 1. First, the powder is added to represent 50% of the feedstock volume. The feedstock is homogenized by the mixing action, and when the torque is stabilized, additional powder is introduced in the mixture, in increments of 2% in volume, until a new stabilization of the torque. When the torque dramatically increases and stays at a high level, it means that the quantity of powder is excessive for the chosen binder and that a homogenization is impossible.

From the measures done during the test, a graph, representing the stabilized torque (i.e. the torque when the mix is homogeneous) versus the powder load expressed as a percentage, is built. It shows two trend lines whose intersection corresponds to the optimal loading rate in powder. The analysis of the example of Fig. 1 is presented in Fig. 2.

Once the composition of the feedstock is optimised for both polymer composition and powder loading rate, the material can be manufactured in large quantities. The feedstock is processed using a Thermofisher Rheomex PTW16 co-rotating twin screws extruder which can generate the optimised raw material on a continuous flow.

2.3. Feedstock characterization

The elaborated material is characterized by its physical and thermal properties, both of which are important for the optimisation of the printing and debinding steps.

The relevant physical properties are the change in shear viscosity with temperature, and the shear rate. A Bohlin Instrument RH2000 capillary rheometer is used to measure these characteristics. With this type of device, the shear viscosity of a given polymer and high loaded materials at a given temperature, is measured as a function of a given shear rate. The combination of the two rheometers available in the lab. Allows to measure a full range of shear rates: from 10^{-5} to 10 s^{-1} for the rotational viscometer, and from 100 to 10^{3} s^{-1} for the capillary rheometer.

Each experimental curve is used to build a model for the viscosity versus shear rate. The model follows a power law expressed as follows:

Table 4
Chemical composition in % mass (elements with <0.01% mass are not mentioned, Fe is the balance) of the different studied powders.

Powder	C	Si	P	V	Cr	Mn	Co	Ni	Cu	Mo	W
0–106 µm	1.29	0.64	0.023	2.96	3.90	0.26	0.67	0.16	0.097	4.81	6.11
0–63 µm	1.27	0.66	0.022	3.01	3.99	0.26	0.79	0.19	0.110	4.85	6.03
0–45 µm	1.29	0.64	0.023	2.96	3.90	0.26	0.67	0.16	0.097	4.81	6.11

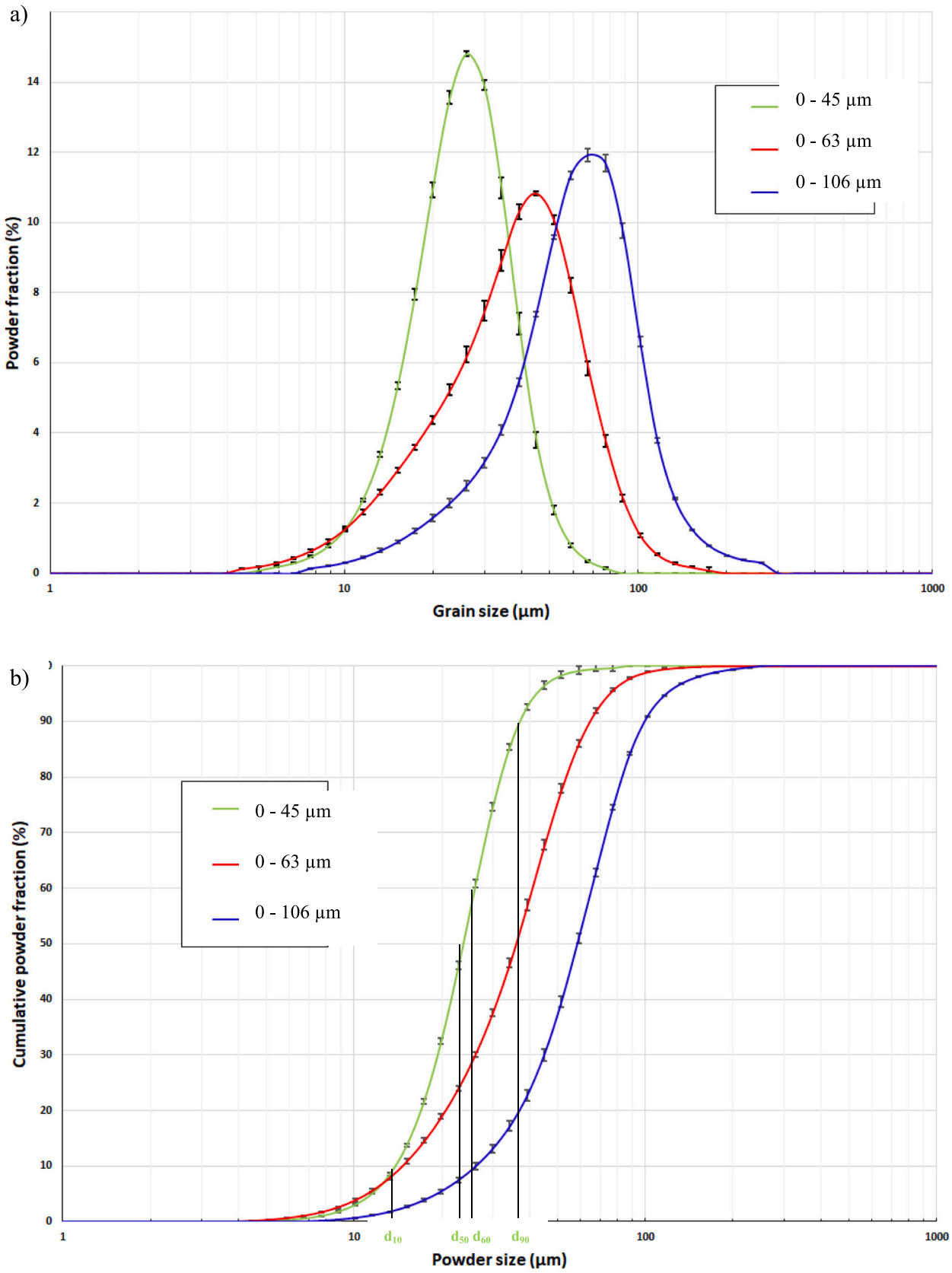

Fig. 4. a) Powder granulometry, b) Cumulative powder granulometry.

Table 5
Shape characteristics of the powders.

Name	Ss ($m^2 \cdot g^{-1}$)	d_{BET} (µm)
0–106 µm	0.0317	23.6
0–63 µm	0.0401	18.6
0–45 µm	0.0491	15.2

Table 6
Powder rheological parameters.

Name	Cu	Fag	S_w
0–106 µm	1.119	2.66	4.409
0–63 µm	1.141	2.47	3.962
0–45 µm	1.097	1.77	5.908

$$\mu(\dot{\gamma}) = K \bullet \dot{\gamma}^{n-1} \tag{5}$$

where μ is the viscosity in Pa.s, $\dot{\gamma}$ is the shear rate in s^{-1}. K the consistency index in $Pa \cdot s^2$ and n is the flow behaviour index are the factors of the law. Pseudo-plastic fluids are also referred to as shear-thinning fluids characterized by $n < 1$.

Viscosity according to the temperature is modelled with the Arrhenius law [29] given in Eq. (6):

$$\mu(T) = B \bullet exp\left(\frac{E_a}{R^*T}\right) \tag{6}$$

where T is the temperature in Kelvin, B is a factor, E_a is the activation energy in $J \cdot mol^{-1}$ and R is the constant of perfect gasses in $J \cdot mol^{-1} \cdot K^{-1}$.

The combination of these models allows the viscosity to be modelled as a function of temperature and shear rate like in the Eq. (7) below:

$$\mu(\dot{\gamma}) = K \bullet \dot{\gamma}^{n-1} \bullet exp\left(\frac{E_a}{R^*T}\right) \tag{7}$$

In the work of Strano et al. in [30] the theoretical window of the optimal parameters for extrusion is determined for 316 L Metal MEX as a function of temperature, shear rate and powder loading using a capillary rheometer and analytical approaches and physical observations. The methodology to determine the shear rate during process and some extrusion printing parameter optimisations have been developed for a pure polymer binder [31] and for MIM pellets [30].

To control the behaviour of the raw material during the shaping process, its thermal characterization is necessary. For that, a DSC 31 evo SETARAM is used to perform a thermodifferential analysis named Differential Scanning Calorimetry (DSC) analysis. DSC analysis highlights the temperature at which specific phenomena happen in the feedstock. Each test is performed on a 0.04 to 0.8 g sample, in a temperature range of 20 to 250 °C, scanned three times, with a heating rate of 3 °C/min.

The DSC analysis reveals temperature peaks corresponding to different binder-related phenomena, such as melting, crystallization or degradation temperatures.

2.4. 3D printing

The different parts are designed by Computer-Aided Design (CAD) and then, imported in a 3D printing control software. The RepeiterHost software is chosen and is coupled with the open source slicer Slic3r. The control software permits to select the printing parameters, such as the nozzle and bed temperatures, the printing and infill strategies. The control software slices the part and converts it into a machine GCODE file, which is transferred to the 3D printer.

The conventional Fused Filament Fabrication (FFF) printers are mature and commercially available; their base materials are a calibrated filament with rigorous mechanical properties. A fused Granular Fabrication printer based on a Distudio3D provider with extrusion head is preferred, as characteristics of granular media are less demanding. The equipment is a screw-based pellet extruder controlled by the screw rotation provided by Direct3D especially studied for MIM feedstock and high loaded polymers. It is a relatively simple design and no feedback ensures the stability of the printing process. The melted feedstock is extruded through a nozzle, which diameter has a significant impact on the shear rate and thus, on the viscosity during the printing stage. The printing speed corresponds to the speed at which the extruder's head is moving; it imposes a necessary extrusion flow. The extrusion speed on the pellet extrusion nozzle is adjusted by means of a multiplying coefficient, called the flow ratio, which is set, in our case, to a value of 125% to obtain a constant flow rate. The molten composite is then extruded

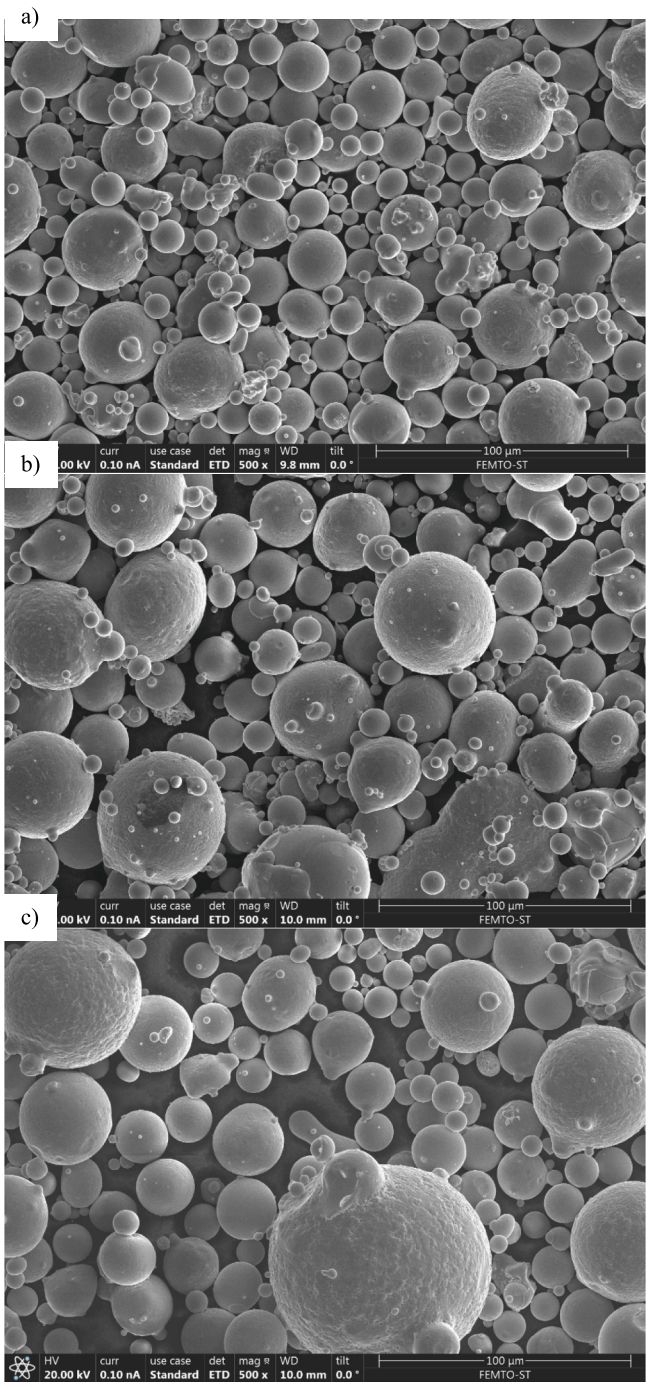

Fig. 5. SEM capture for a) 0–45 µm powder size, b) 0–63 µm powder size and c) 0–106 µm powder size.

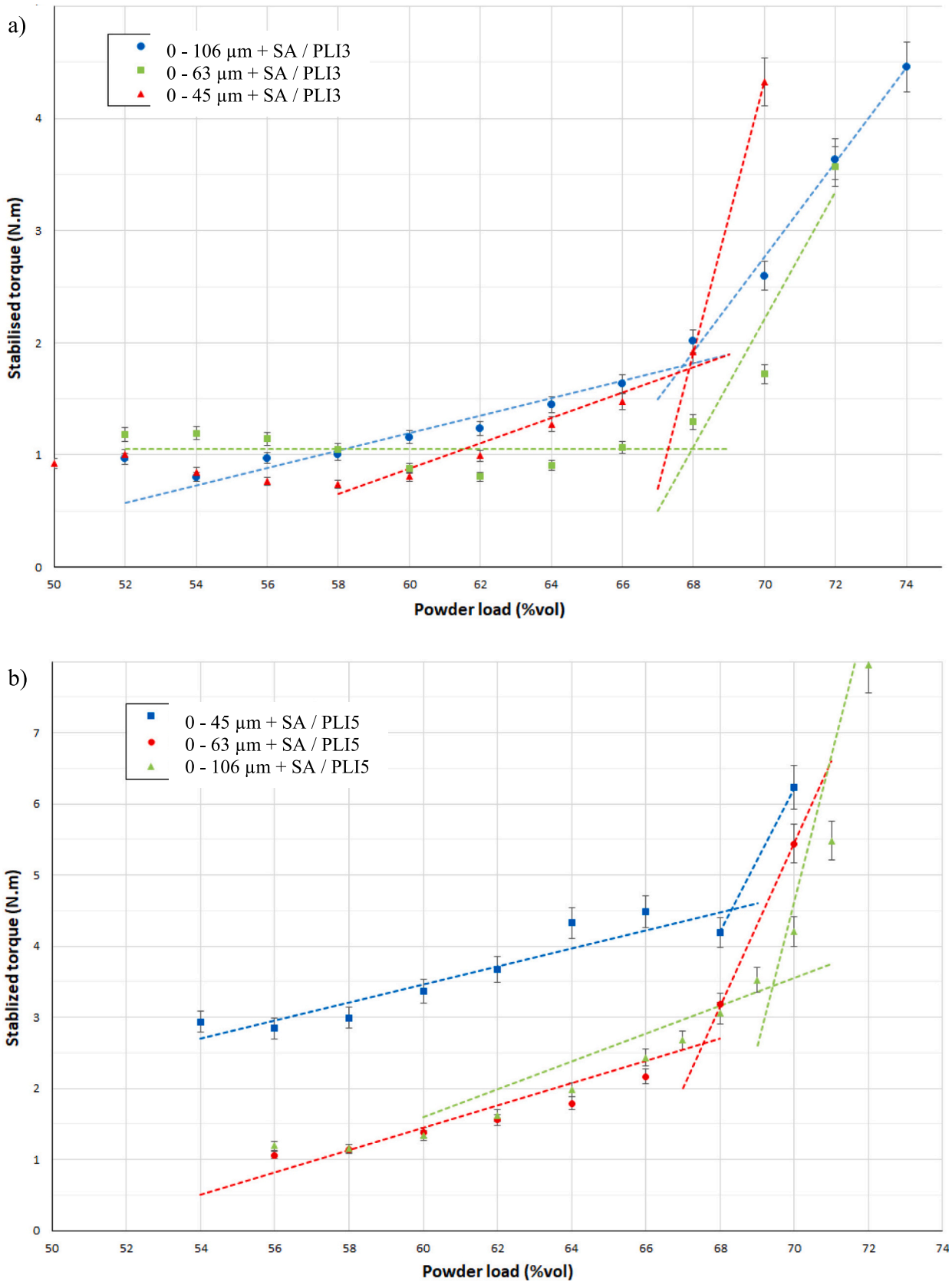

Fig. 6. Influence of the powder for a) PLI3 and b) PLI5 as backbone.

Table 7
Surfactant to powder surface.

	Ss ($m^2.g^{-1}$)	SA proportion (%w)	*Sc* ($mg{\cdot}m^{-2}$)
0–106 μm	0.0317	0.4797	162
0–63 μm	0.0401	0.4797	128
0–45 μm	0.0491	0.4797	105

and deposited, layer by layer, on a printing plate, by moving the extrusion head at printing speed to elaborate printed components.

All the parameters need to be optimised as nozzle diameter and printing speed for each granulate material to produce dense parts. To do that, a Design of Experiment (DoE) is carried out. The layer height is chosen such as its maximal value corresponds to between ¼ and ½ of the nozzle diameter, leading to a value of 0.3 mm for the height [32]. The selected nozzle presents a diameter of 0.8 mm corresponding to a printing depth of 0.3 mm. Printing speeds range from 10 to 40 $mm.s^{-1}$. The maximum speed is suitable for biomaterials with a low plant fibber content, while for PLA grades with a high powder content, conventional printing speeds are rather low (i.e. between 10 and 20 mm/s), see Benie et al. in [33]. Using the same equipment as N'dri et al.in [34], a variety of highly-filled magnetocaloric powder composite parts were printed without any problems and with a high degree of homogeneity. Finally, the possible maximal volume of fabrication is a 350 × 250 × 250 mm^3 prism.

2.5. Thermal debinding

In the literature, for thermal debinding, the mean time is of 69 h with a lowest time of 18 h. In case of solvent debinding, where the creation of porosities networks is observed, it is mandatory to combine it with thermal debinding to complete the removal of the binder. In this case, the combination of the two methods (thermal and solvent) will result in a shorter kinetic time cycle than pure thermal debinding. The mean time is of 28 h with the lowest of 15 h; in Table 11, several studies with a debinding time of around 19 h was observed. In the case where the supercritical CO_2 method is employed, debinding time is really shorter with a duration of about 8 h. The debinding time resulting from our study is of 16.5 h, which is quite short compared to the duration presented in Table 1.

Table 1 lists different feedstocks used in PIM and their respective debinding time cycles. Table 1 collects some data presented in an article of Rolere, Soupremanien et al. [35] completed with others. We focussed only on experimental results where the debinding protocol was

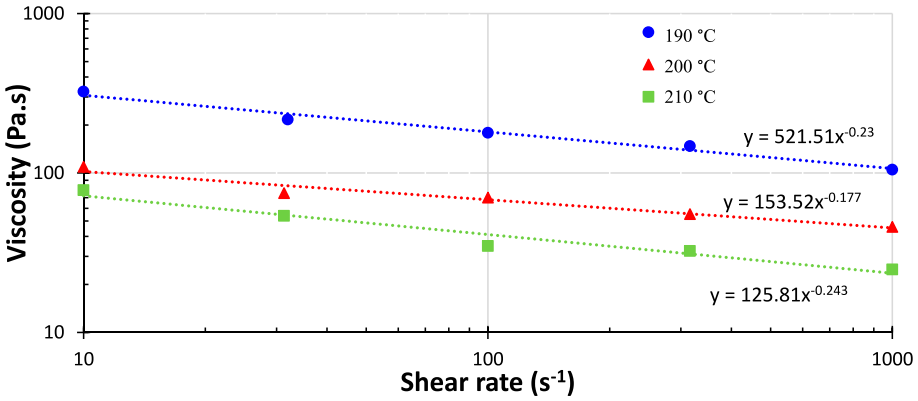

Fig. 7. Viscosity vs shear rate at 190 °C, 200 °C and 210 °C for the PLI5 feedstocks for the powder with a granulometry of 0–45 μm.

Table 8
Identified parameters of the power law according to the temperature for the different feedstocks referenced by their granulometry.

Temperature	190 °C		200 °C		210 °C	
Parameters	K	n	K	n	K	n
0–45 μm	521	0.770	153	0.823	125	0.757
0–63 μm	520	0.714	428	0.725	35	0.865
0–106 μm	344	0.832	738	0.617	339	0.458

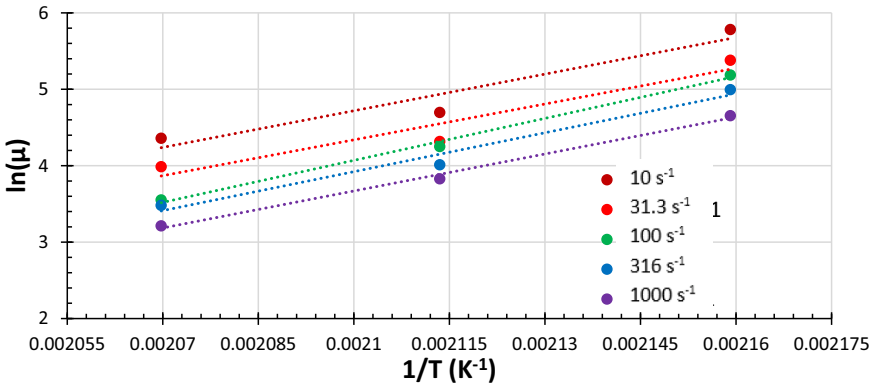

Fig. 8. The logarithmic viscosity vs. the inverse of the temperature for of the feedstock 0–45 μm.

Table 9
Parameters of the Arrhenius law.

Name	B	E_a (kJ·mol^{-1})
0–45 µm	$1.63 \cdot 10^{-13}$	135
0–63 µm	$8.66 \cdot 10^{-17}$	161
0–106 µm	$2.06 \cdot 10^{-7}$	157

completely documented.

The debinding parameters are measured with the STA 449C Jupiter Thermo-scale by the Netzsch company, where the thermo-scale is used as a coupled thermogravimetric analysis (TGA) and DSC. TGA measures the mass variation during the heating of the sample. The onset temperature of the binder degradation (*Tdo*) happens at the same time where the mass loss starts. The temporal derivative of this mass loss presents a peak corresponding the optimal degradation temperature (*Tdp*).

The selected temperature for the debinding stage is slightly higher than the *Tdp* and is limited by the equipment. Additionally, the debinded samples are analysed by TGA to validate the complete binder degradation.

A France Etuve XU27 oven is employed for debinding the various printed components. Its maximum temperature is 300 °C, and the temperature cycle is carried out in a neutral Argon atmosphere to avoid oxidation. The debinding cycles are defined according to the optimal temperature, the component size and the binder composition.

2.6. Densification

The densification is realized by natural sintering. The sintering characteristics are measured with a dilatometer Setsys from SETARAM. The dilatometer measures the shrinkage during the thermal cycle as a function of the chosen kinetics and the selected atmosphere. The thermal cycle is performed on debinded samples, heated to 1100 °C with a 50 °C·min^{-1} temperature rise rate, and then to 1300 °C with a 25 °C·min^{-1} heating rate. The result is a graph representing the sensor position versus the temperature, from which its derivative with respect to time reveals the range of the sintering temperature. However, this range of temperature does not necessary assure to get a partial fusion for joining powder grains together and to maintain the required part

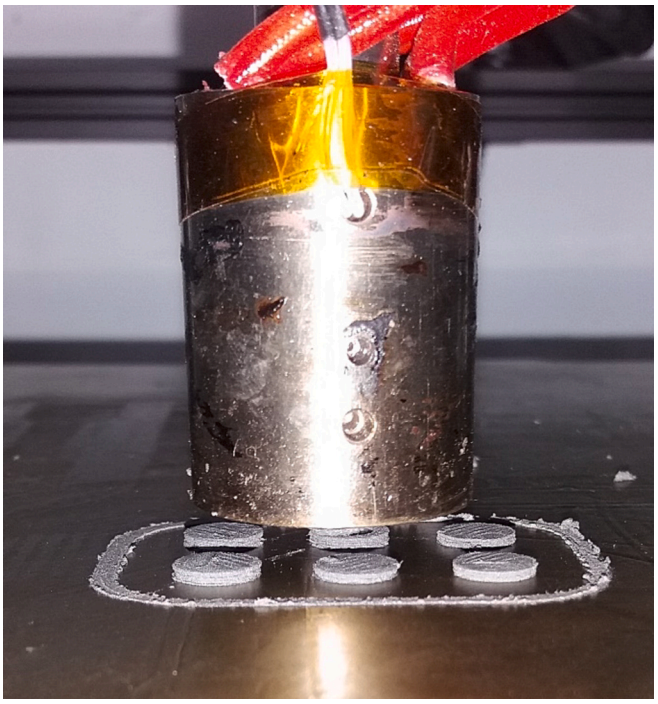

Fig. 10. Ongoing printing of a batch of cylinders.

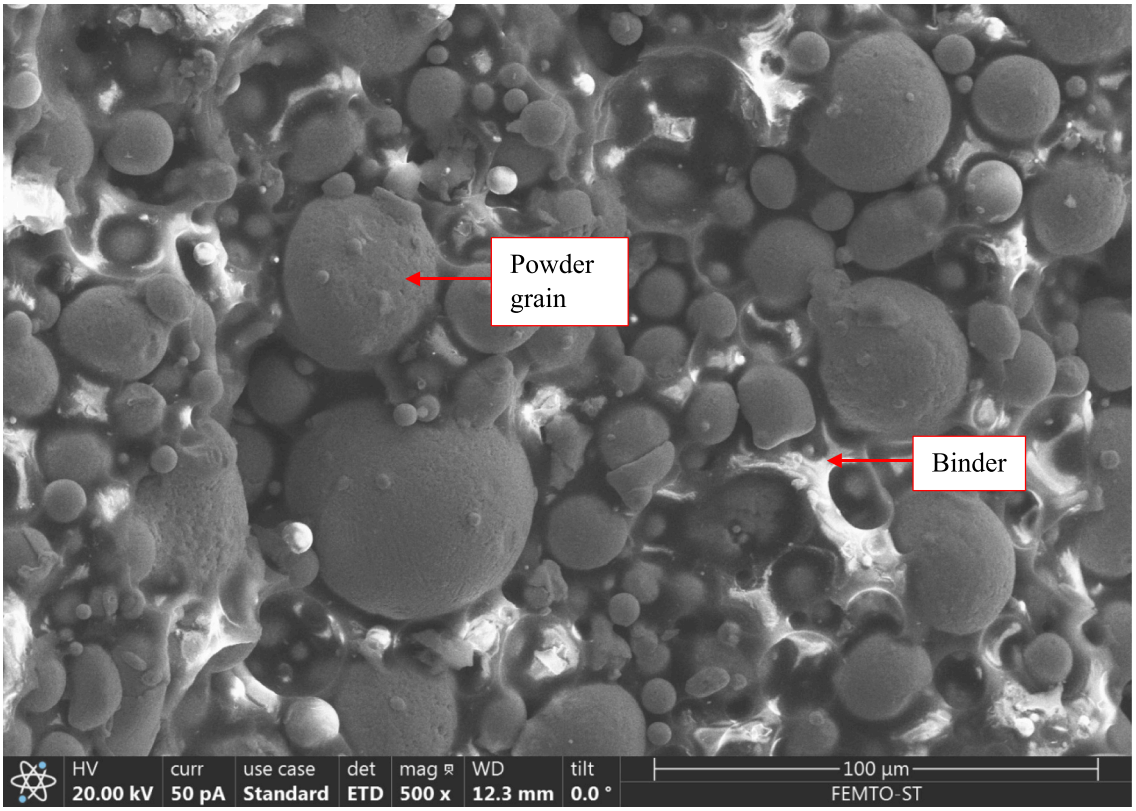

Fig. 9. SEM capture of a 0–63 µm PLI5 feedstock granulate.

Table 10
Presentation of the DoE for all three feedstocks (0–45 μm, 0–63 μm and 0–106 μm) used to optimize the set of parameters (nozzle temperature and printing speed) of the printing stage, together with the results obtained in terms of density and dimensional accuracy (nozzle diameter is 0.8 mm, printing depth is 0.3 mm).

Set of parameters N°		1	2	3	4	5	6
Nozzle Temperature (°C)		190	190	200	200	210	210
Printing Speed (mm·s^{-1})		10	20	10	20	10	20
0–45 μm	Density (g·cm^{-3})	FTP	FTP	4.323	4.125	4.134	4.194
	Dimensional variation (%)			5.6	6.2	7.7	9.6
0–63 μm	Density (g·cm^{-3})	3.883	4.089	4.118	4.125	4.228	4.157
	Dimensional variation (%)	3.6	5.0	6.9	10.3	14.6	7.3
0–106 μm	Density (g·cm^{-3})	FTP	FTP	3.916	4.206	4.312	4.145
	Dimensional variation (%)			4.6	9.5	15.0	19.4

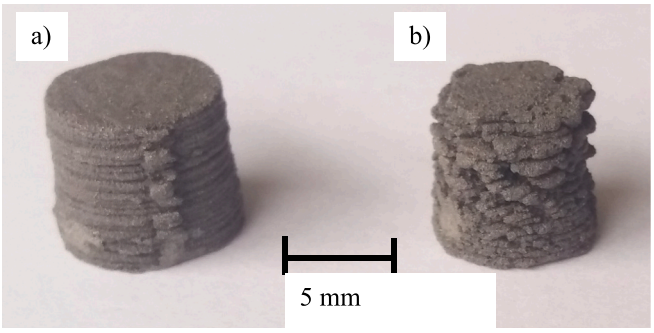

Fig. 11. Parts printed with 0–106 μm feedstock material with a) set parameters no. 4 giving a suitable cylindrical geometric shape and b) set parameters no. 2 giving a print failure.

geometry by avoiding melting. Once the ideal temperature is obtained, further tests are run to define the optimal sintering temperature and holding time; longer holding times generally lead to higher final densities and allows the pore elimination and microstructure rearrangement [48].

2.7. Specimen characterization

At this stage, it is important to examine the porosity. It is a very influential parameter for the component's mechanical specifications. Moreover, it is essential to ensure that all the opened porosity has been well eliminated (usually lower than 5%) in order to apply a Hot Isostatic Pressing (HIP) post-treatment to produce a fully dense part. Several methods permit such measurement.

The density measurement with hydrostatic double weighting is the easiest way to evaluate the porosity. The sample is first weighed in the air, and plunged into ethanol. The buoyancy of the sample in ethanol creates a difference of weight that is used to calculate the part volumetric mass. The comparison of this volumetric mass to the volumetric mass of the powder material gives a difference, which is caused by the inside porosity. It is the most accurate method for density measurement.

Another method consists of cutting the samples and observing, after polishing, the pores with an optical microscope. By coupling the microscope with an image analysis software (like the Keyence suit, used in the present work), it is possible to calculate the sample's porosity; moreover, it can qualify the pore size distributions and their localisation. The main drawback of this measure is its destructive nature and its local validity. Moreover, microstructural and morphological characterizations of powders and sintered parts are performed by scanning electron microscopy (SEM - JEOL 7610 F SEM-FEG) in secondary and backscattered electrons imaging. Qualitative chemical compositions of the phases are identified by energy dispersive X-ray spectrometry (EDS).

The last method is tomography. The part is submitted to X-rays with multiple angles and an analyser permits to get different slices of the part. With the help of a reconstruction software, a 3 D model of the component, describing its exterior and interior, is obtained revealing the internal voids. It is an expensive analysis, but it is non-destructive and it gives a complete representation of the pores size and localisation. Tomography analyses are done on an Easytom RX Solution tomograph of the MIFHYSTO mutual technical centre. The reconstruction is analysed to determine the pore distribution. In addition, to evaluate the surface quality of sintered specimens, the longitudinal roughness is measured with an *ALTIMET Altisurf 520* every 90° for each part. The measured profiles are discretized, and filtered with a Gaussian filter considering a cut-off of 2.5 mm.

2.8. Polymer

In FFF, the two main polymers used for printing are Acrylonitrile Butadiene Styrene (ABS) and PLA. While ABS is based on petroleum, PLA is a bio-sourced polymer, obtained from corn starch; the starch is eaten by bacteria creating lactic acid, which is polymerized in a further process. So, PLA is chosen as it is commercially available, well suitable for 3D printing and has been already studied in the lab [13].

PLA is a stereoisomeric polymer which can have a cis/trans orientation, depending on the isomer used for the synthesis: either (L)-lactic acid or (D)-lactic acid can be polymerized into Poly-L-Lactic-Acid (PLLA) and Poly-D-Lactic-Acid (PDLA) respectively, when they are

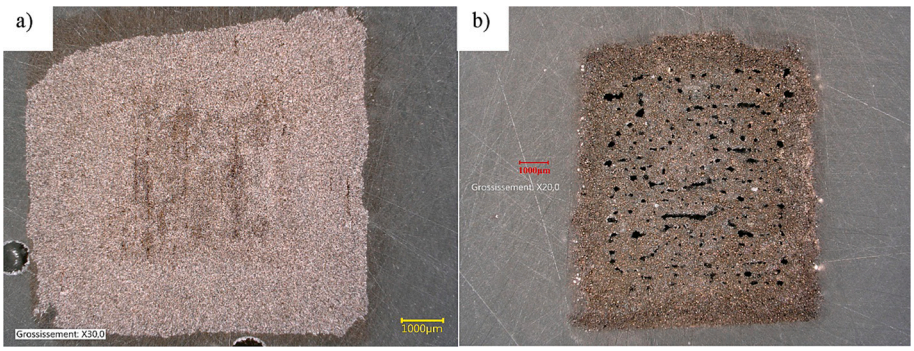

Fig. 12. Cross section of a debinded cylinder for a) PLI5 and b) PLI3 based feedstock.

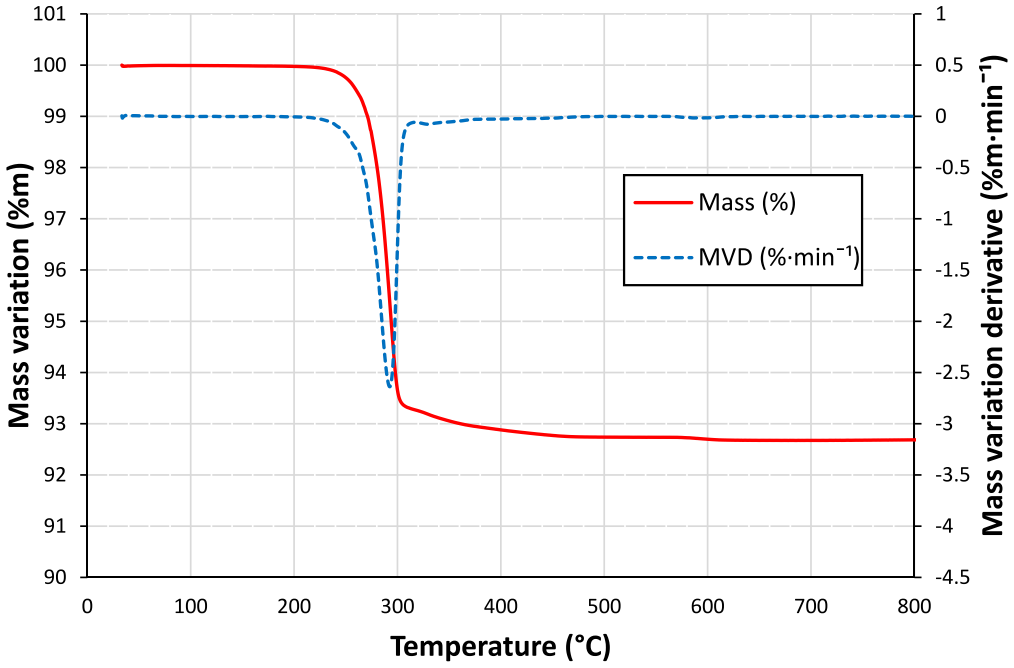

Fig. 13. TGA result of printed matter for the PLI5 based feedstock, from 25 °C to 800 °C with a 10 °C/min kinetic. MVD is the Mass Variation Derivative.

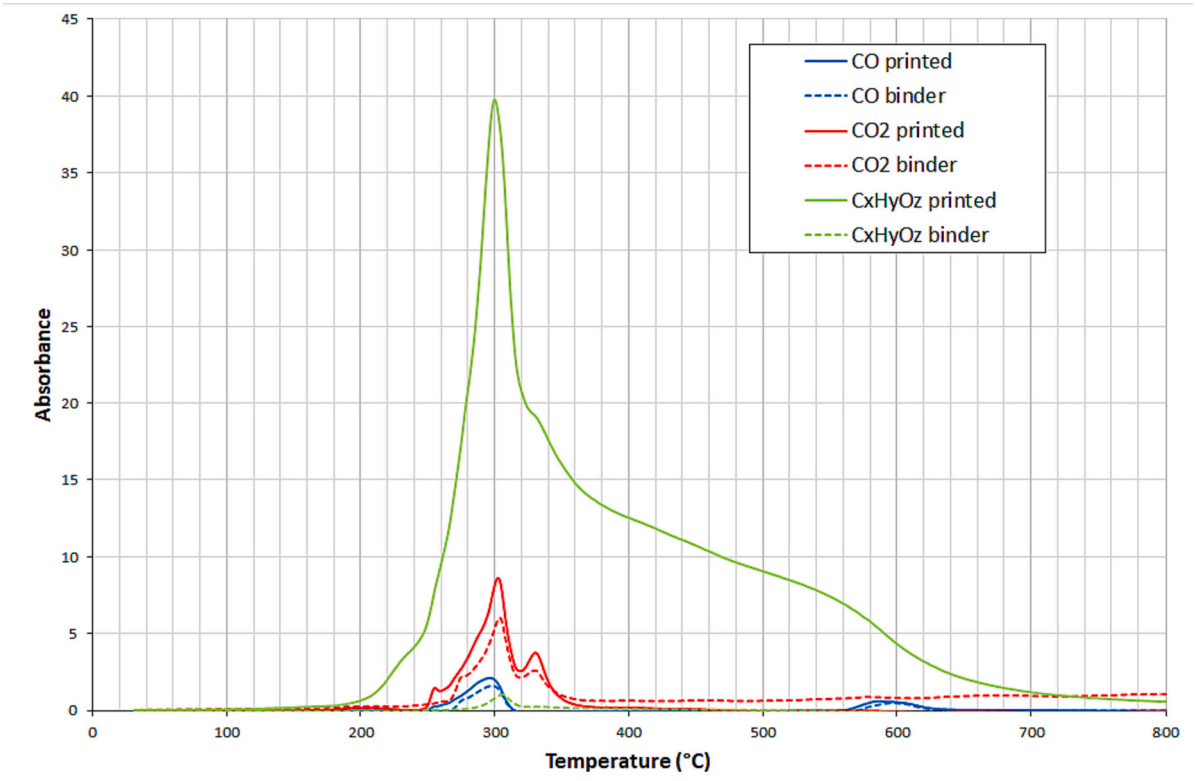

Fig. 14. Infrared spectroscopy of gas during the TGA test, from 20 to 800 °C with a 10 °C·min^{-1} kinetic.

pure; in case of a mix of the cis- and trans-lactic acid, one gets a Poly-DL-Lactic-Acid (PDLLA).

PLA in its pure form (PLLA or PDLA) presents a semi-crystalline behaviour for its α form, with a glass transition temperature (*Tg*) of 60 °C and a melting temperature (*Tm*) of 175 °C. PLLA can also crystallize in a β structure; in that case, its fusion temperature raises up to 185 °C.

For its part, the PDLLA follows an amorphous behaviour.

PLA is commercially available from Natureplast company, which proposes different grades listed in Table 2.

PLA is the backbone for the development of the bio-sourced binder, but its low powder load capacity and its high viscous behaviour do not permit to use it alone. A wetting agent is necessary, whose role is assured by a large variety of components. The saturated fatty acid family is usually used, where saturated fat such as Stearic Acid (SA) or Palmitic Acid (PA) are extracted from alimentary oils; for example, cocoa butter

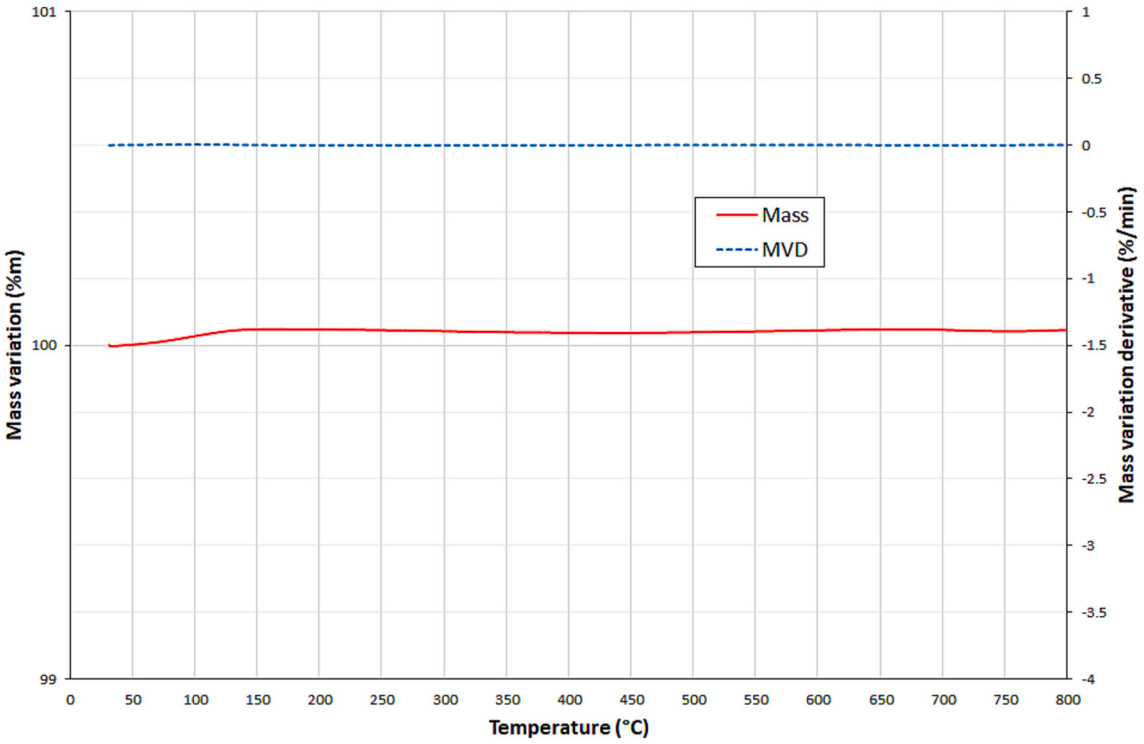

Fig. 15. TGA result of debinded matter, from 25 °C to 800 °C with a 10 °C·min^{-1} kinetic. MVD is the Mass Variation Derivative.

Table 11
Porosity evolution.

	Low porosity (Fig. 16 a)	Controlled porosity (Fig. 16 b)
Printed part porosity (% vol.)	0.03 ± 1	0.88 ± 1
Debinded part macro-porosity (% vol.)	4.97 ± 1	0.52 ± 1

contains 35% of SA and 27% of PA, palm oil contains 5% of SA and 44% of PA. These components are refined and are composed from a single molecule. SA is a reference wettability bio-sourced agent [49]; it is chosen in the present development and comes from Merck KGaA.

The DSC analysis presented in Fig. 3 shows the behaviour of the different binder components vs the temperature. An increase in heat flow corresponds to an exothermic reaction, while a decrease corresponds to an endothermic one. For a polymer, an endothermic increase to a plateau corresponds to a glass transition temperature (*Tg*), an exothermic peak corresponds to a crystallization temperature (*Tc*) and an endothermic peak corresponds to a melting temperature (*Tm*). For other materials, an endothermic peak corresponds to a melting temperature (*Tm*). The feedstock binders are composed of two materials and multiple characteristic temperatures are observed. Fig. 3 presents the normalized heat flow for the selected binder's components.

The measured characteristics are quite different from the one given in the supplier datasheet; the melting temperature of the PLA is found to be lower than the one announced. The characteristic temperatures of the mix PLA-surfactant are lower than the ones of the two separate components. Table 3 shows the measured characteristics of the components, averaged with 3 cycles.

The DSC analysis of the binder components shows the endothermic peaks, at 72 °C corresponding to the SA melting temperature and at 171 °C and 178 °C corresponding to the PLA melting temperature; exothermic peaks corresponding to the PLA crystallization temperature is observed at 80 °C for the PLI5 and 108 °C for the PLI3. The binder presents different characteristics; with a mix of the backbone PLA and the surfactant SA, the temperatures are lowered, with a melting of the SA at 67 °C, a crystallization of the PLA at 80 °C and a melting of the PLA at 165 °C.

2.9. Metallic powder

The core material of the powder used in this study is a tool steel named ASP2023, which can be found under the name AISI M3–2 and is designated as EN - X128WMoCrV6–5–4-3. The powder comes from three different atomization batches; each batch is passed through different sieves. They are referenced by the sieve's mesh size: 0–45 μm, 0–63 μm and 0–106 μm.

As each powder comes from different atomization batches, their chemical composition presents some variations as revealed by the figures in Table 4, measured according to the ASTM-E1019 standard.

The measured volumetric mass is 8.04 g.cm^{-3}.

3. Results and discussions

3.1. Powder characteristics

In order to study the influence of the powder particle size on each stage of the process, three particle size classes were prepared by sieving. The different analyses of these powders are presented in Fig. 4.

The Fig. 4 a) reveals that the three powders present a single-mode distribution, centred around a size of 24, 36 and 58 μm respectively. However, only the 0–63 μm powders present a non-symmetrical distribution in size due to a larger number of small particles. Nevertheless, our selection seems to be pertinent as shown Fig. 4 b) to evaluate the influence of the particle size on the fabrication of parts from the powder to the massive.

The particle size distribution (PSD) is obtained from Fig. 4 b); the PSD can be directly read on the graph, as the intersection between a straight line at X% and the observed cumulative powder line, giving a d_x which corresponds to the powder size on the abscissa.

The shape parameters of the different powders are given in Table 5. The specific surface is measured from a powder sample of 11.9 to 13.6 g,

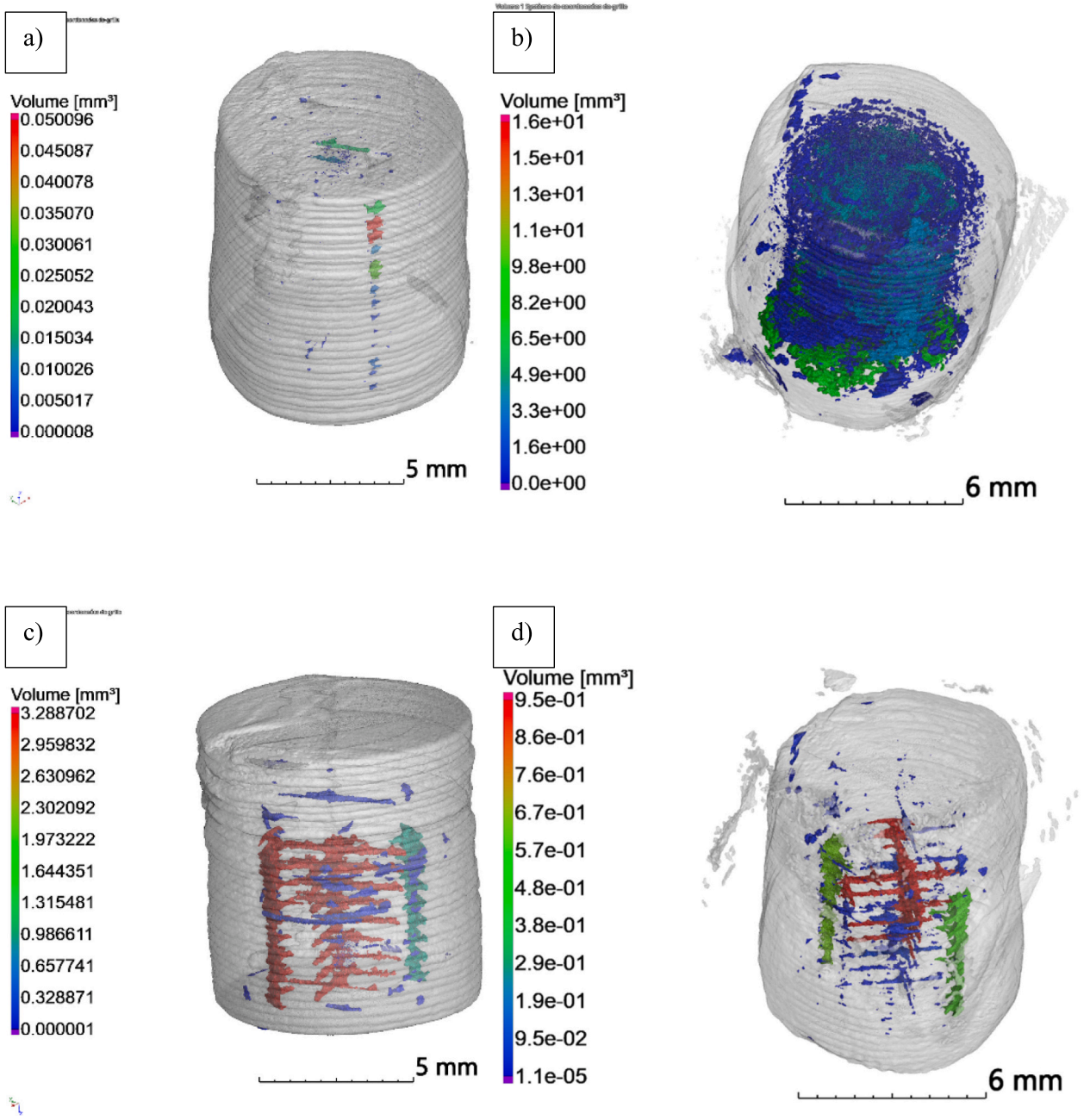

Fig. 16. Tomographic reconstruction part before and after debinding for a) a low porosity sample before debinding, b) and the low porosity sample after debinding; c) for a controlled porosity sample before debinding and d) for a controlled porosity sample after debinding.

with a preliminary desorption cycle of 4 h at 250C.

The nominal specific surface area of a uniform powder with a diameter equal to d_{50} is smaller for the three studied powders; this is due to the asymmetry in the grain size distribution, where d_{50} is not centred at the top of the Gaussian curve.

The coefficient of uniformity (*Cu*), the agglomeration factor (*Fag*) and the distribution slope parameter (S_w) have been calculated with Eqs. (1), (2), (3) and (4) respectively, for the three batches named 0–106 μm, 0–63 μm and 0–45 μm. The data are grouped in Table 6.

With a C_u <6 and a *Fag* just slightly above 1, it results that the chosen powders present a uniform distribution and do not contain agglomerates.

Finally, as $S_w > 4$, the studied powders display a reduced distribution which could compromise their flow [50].

Finally, SEM analyses (Fig. 5) according to the ASTM E2142–08 standard permit the observation of the shapes of the powder grains. For the three powder batches, the grains are mostly spherical, even if some oblong grains can be observed. Some satellites are present, and their surface is smooth despite some peeling texture. Visibly, the powder distribution appears to be as wide as measured by laser diffraction, with grains ranging from 5 to 30 μm in diameter in Fig. 5 a), from 5 to 50 μm in diameter in Fig. 5 b) and from 5 to 100 μm in diameter in Fig. 5 c).

3.2. Feedstock development

The binder is composed of PLA as backbone, and SA as wettability agent, in a 90 to 10% vol. ratio. This high SA content is chosen to ensure an excess of SA in reference to the article [51], where it is shown that a 5% of SA in the binder guarantee an optimal feedstock of a 17–4PH powder with PW-based binder.

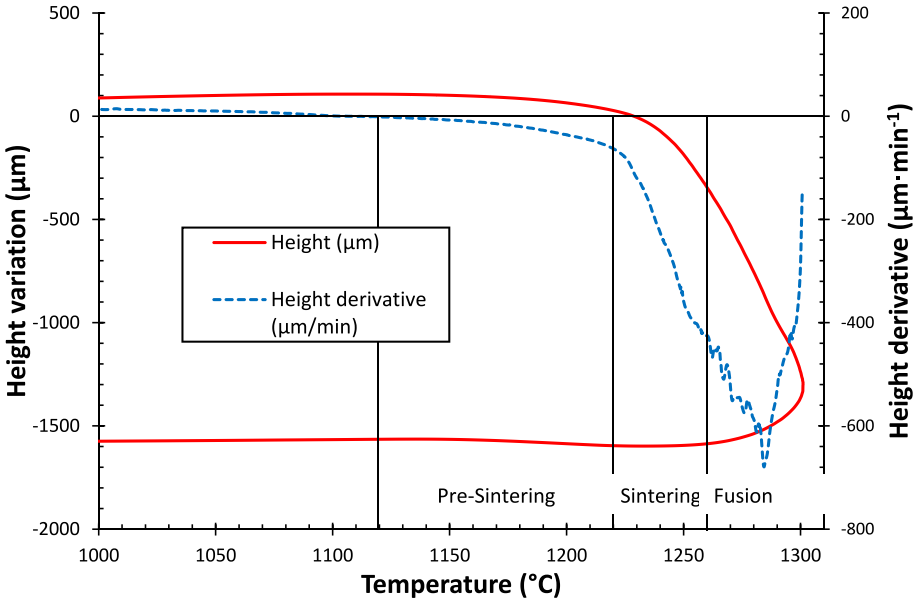

Fig. 17. Dilatometry of the 0–45 µm powder, zoom on the 1050 to 1300 °C temperature range.

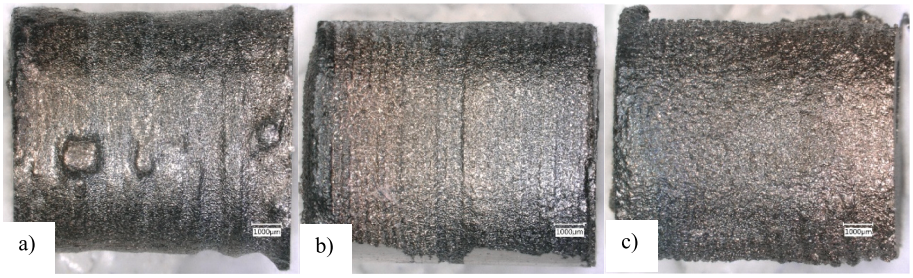

Fig. 18. Samples after sintering at 1250 °C during 2 h of a) 0–45 µm, b) 0–63 µm and c) 0–106 µm powders.

The starting feedstock based on this binder is developed using the incremental mixing method presented in section 1.2, whose analysis is presented in Fig. 6 a) and b), for a binder based on the PLI 3 and PLI 5 grades, respectively. The Fig. 6 shows that the powder size does not have a specific impact on either the critical loading rate or the torque. The critical loading rate is 68%vol for each powder size and binder.

So, feedstock has been produced with the following composition: PLA (PLI3 or PLI5) 28.8% vol., SA 3.2% vol., Powder 68% vol. This high loading rate is interesting, as it will produce a low shrinkage during the sintering stage.

3.3. Feedstock characteristics

The surfactant plays the role of a wetting agent between the powder and the backbone polymer, and a minimal quantity is needed to encapsulate fully the powder grain. The surfactant concentration in the feedstock can be evaluated from the knowledge of the powder specific surface and the imposed loading rate. The resulting surfactant concentrations (Sc) are presented in Table 7.

As described in Table 7, the Sc in SA range from 105 to 162 mg·m^{-2}. Comparing this concentration to the work of T. Hanemann and R. Heldele in [49] with a PE-PW binder, the created feedstock includes an important quantity of surfactant, while a concentration higher than 2.2 mg·m^{-2} has little if any effect on the feedstock viscosity. Auscher et al. in [52] found that for a feedstock based on a PE Low Density, the optimal SA concentration is of 1.9 mg·m^{-2} only. That means that, even if PLA-based feedstock needs higher surfactant concentration, the SA proportion in the present feedstock could be reduced by a factor 50 without changing its effect; an excess of surfactant is still insured.

Fig. 7 presents the feedstock viscosity measured for different shear rates at different temperatures. As the typical shear rate in printing process is of 100 s^{-1}, five values between 10 and 1000 s^{-1} have been explored. The considered temperatures are 190 °C, 200 °C and 210 °C with granulometry (0–45 µm) in Fig. 7. These temperatures are above the melting point and below the degradation temperature. Measurements are done using a 2 mm diameter by a 16 mm height die. Only the PLI5 based feedstock is measured as the PLI3 based feedstock is not qualified for the debinding stage (see 2.5).

All measurements are used to calculate the parameters of the power law and the Arrhenius law. Fig. 7 permits the extraction of the parameters of the power law, grouped in Table 8. For the three feedstocks and the selected temperatures, the *n* factor is inferior to 1, indicating that the feedstocks possess a pseudo-plastic behaviour.

The Arrhenius law is determined by extracting its parameters according to the temperature; the graph in Fig. 8 shows the different powder viscosity according to the temperature.

The study of the evolution of logarithmic viscosity as a function of the inverse of temperature leads to the determination of the value of the activation energy. In fact, this value is obtained by multiplying the slope of Fig. 8 by the value of the perfect gas constant. The parameters of the Arrhenius law are given in Table 9 for the three feedstocks. The activation energy increases from the 0–45 µm feedstock to the 0–63 µm feedstock, but shows no significant change between the 0–63 µm feedstock and the 0–106 µm one. This can be observed in Fig. 8 where the viscosity is affected uniformly according to the temperature. It takes more energy (an increase from 190 °C to 210 °C) to affect the feedstock,

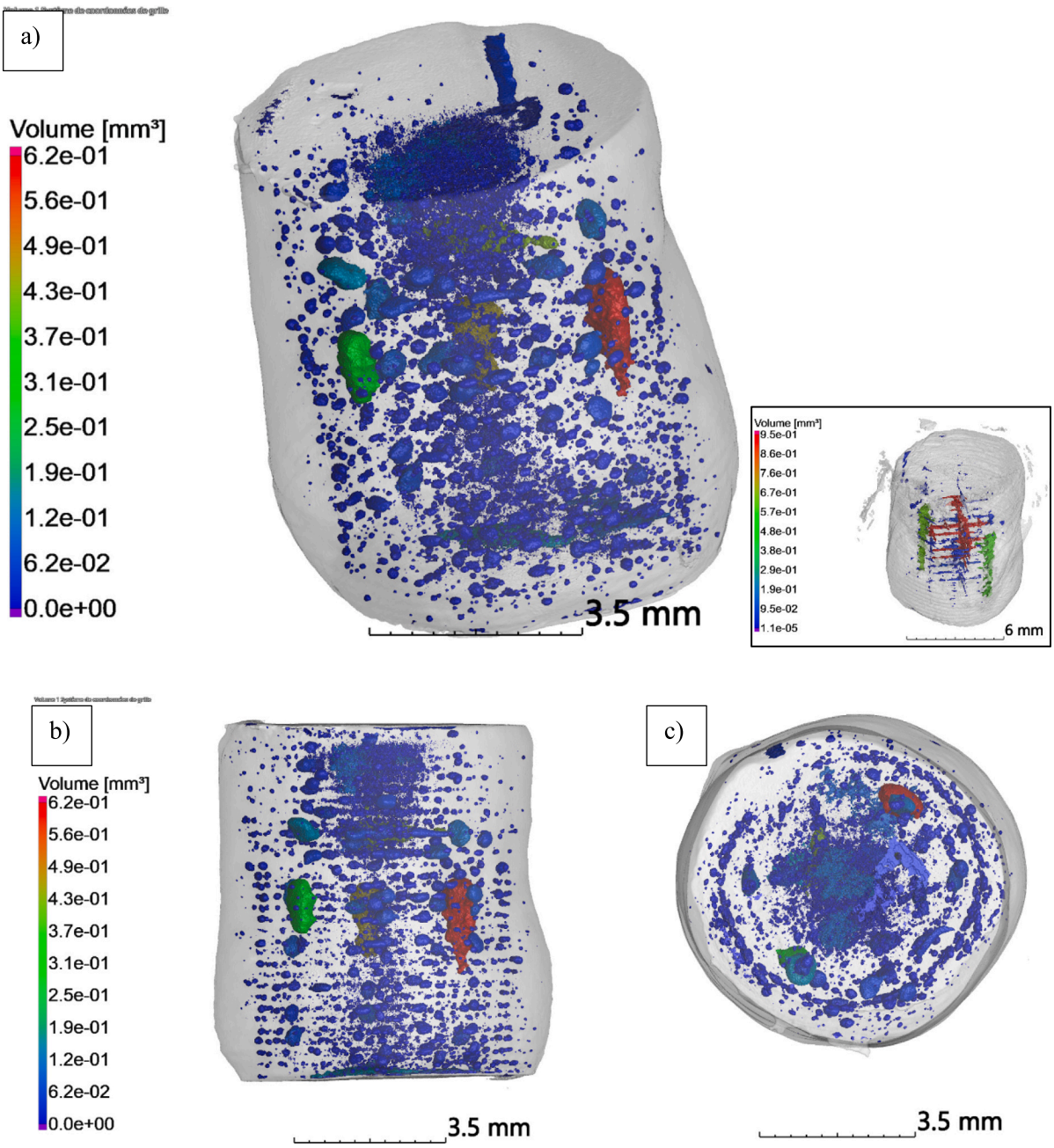

Fig. 19. Tomographic reconstruction of a sintered part from 0 to 63 μm powder with a controlled porosity during printing stage. a) Isometric view, with the tomographic analysis after debinding in medallion, b) face view and c) top view.

Table 12
Evolution of the porosity and *Z*-shrinkage after a sintering at 1250 °C during 2 h for all powders.

Characteristic / Powder	0–45 μm	0–63 μm	0–106 μm
Porosity (%)	2.76	4.54	6.20
Z shrinkage (%)	13.35	13.44	13.91

as the activation energy is higher for those feedstocks.

The model described in Eq. (6), with the parameters given in Table 9, is presented in Fig. 8, and compared to the measures. Additionally, the coefficient of determination R^2 is calculated. The correlation between model and measurement, expressed by R^2, shows a high correlation between experimental data and the analytical model for the 0–45 μm feedstock with a $R^2 > 0.92$. For the 0–63 μm feedstock, the correlation is lower for 200 °C and 210 °C, with a $R^2 > 0.87$. For the 0–106 μm feedstock, the 200 °C temperature presents the lowest correlation with a R^2 of 0.81, while the other two temperatures present correlations superior to 0.93.

Microscopic observations in Fig. 9 show that the powder grains are well wrapped with the binder. The feedstock appears to be saturated, with no segregation phenomena i.e. no large pockets of polymer or unwrapped powder particles. The photography for the 0–63 μm PLI5 feedstock presented in Fig. 9 is representative of the different feedstock used in the present study.

3.4. Printing

Printed samples consist of a cylinder of 8 mm-diameter by 8 mm-height. These small cylinders are used for the determination of the

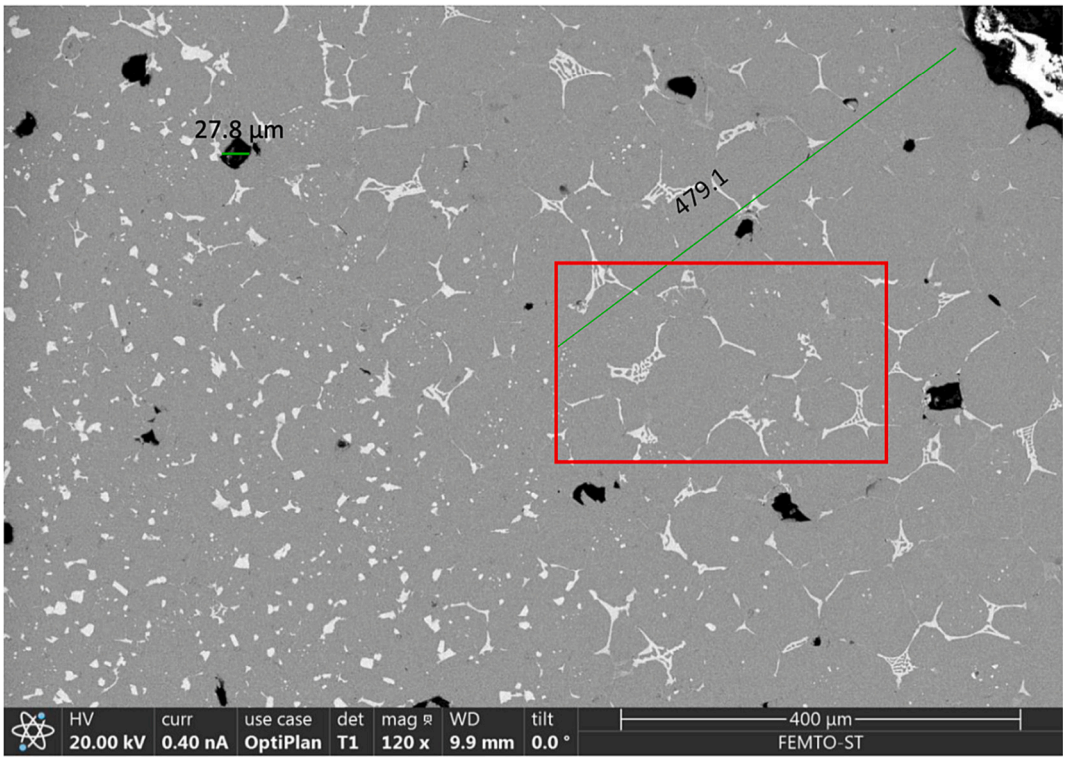

Fig. 20. SEM observation of a cross-section of a sample with a dwell time of 2 h. In red the area presented in Fig. 21.

optimal printing parameters, and also, for the optimisation of the debinding and densification steps. A photograph of the ongoing printing process is given in Fig. 10.

The printing strategy defines the path the print head follows in order to generate the desired geometry. The high geometric accuracy is generally ensured by a two-step printing strategy: first, the outline of the part is created, then the interior of the part is swept by the print head. The part contour can be realized with one or more paths; two paths are chosen in the present work. The part's filling is done with 0 / 90° paths.

The printing temperature has an important influence on the shaping stage, but it is limited by the melting and degradation temperatures of the polymer. Thus, for the considered polymer, the temperature ranges from 185 °C to 220 °C.

Controlling the porosity during the printing stage is essential as it influences the following steps (see part 2.6).

Many parameters have to be considered for the optimisation of the printing stage, like the nozzle and bed temperatures, the nozzle diameter, the printing speed, the layer height. Nozzle temperature and printing speed are the most important parameters. The others present less influence, and their values can be fixed. Concerning nozzle temperature, it has a direct influence on the feedstock viscosity. For the bed temperature, it is chosen according to the general specification of the PLA supplier for MEX, which indicates a bed temperature of 60 °C, higher than the binder's *Tg,* which insures the maximal adhesion force [53].

These parameters are optimised with a DoE method where the conditions of the necessary tests are given in Table 10, as well as the results according to the density of the parts and their respect to the imposed geometrical dimensions. At 190 °C the printing process results in failure to print (FTP) for the 0–45 µm feedstock.

Components printed with feedstock 0–106 µm are illustrated for two sets of parameters (set number 2 and 4) in Fig. 11. The first set (number 2) leads to a printed component with defects and the second set (number 4) leads to a printed component with a suitable geometrical shape without the presence of external defects.

The DoE shows that a single set of parameters results in differences for each feedstock. For the 0–45 µm and 0–63 µm feedstock, the results are the best with a nozzle temperature of 200 °C and a printing speed of 10 mm·s^{-1}. For the 0–106 µm feedstock, a nozzle temperature of 200 °C and a printing speed of 20 mm·s^{-1} define the best conditions.

3.5. *Thermal debinding*

Preliminary tests have been led on printed parts to observe the behaviour of the parts during the debinding stage. They show that PLI3 grade is too fluid for retaining the part shape during the debinding stage, even if the debinding operation is conducted in an alumina powder bed to help retaining the shape, the final geometry was not satisfying. In Fig. 12, the cross section of printed and debinded cylinders with a PLI5 and PLI3 based feedstock are compared showing an important deteriorated internal structure where the PLI3 filler is used; internal macropores can be observed in Fig. 12 (b). Lowering the debinding kinetics has no effect on the deterioration of the internal structure of the PLI3-based feedstock.

In order to optimize the debinding process, a TGA is performed to identify the optimum debinding temperature. From a sample of 584 mg of printed material, the result shown in Fig. 13 is obtained.

The material degradation is done in two steps. A first degradation starts at 190 °C and ends at 460 °C, with a loss of 7.26%w; a peak of degradation is observed at 292 °C, corresponding to the degradation of the majority of the polymer. Another component is decomposed between 560 and 630 °C, with a loss of 0.05%w; it could be an additive in the material or any lubricant present in the device.

From this TGA, it can be concluded that 87% of the degradation is completed at 300 °C. This temperature is then selected for the debinding step. The debinding starts with a quick heating to 150 °C in 0.5 h as the binder does not melt yet, followed by a slow increase up to 300 °C with a thermal kinetic of 10 °C·h^{-1} and a holding time fixed at 1 h. The debinding cycle time (without cooling) is of 16.5 h. Additional TGA tests are performed on debinded samples to check if the thermal degradation is sufficient, as it is shown in Fig. 15 .

The infrared spectroscopy presented in Fig. 14 shows in solid line the

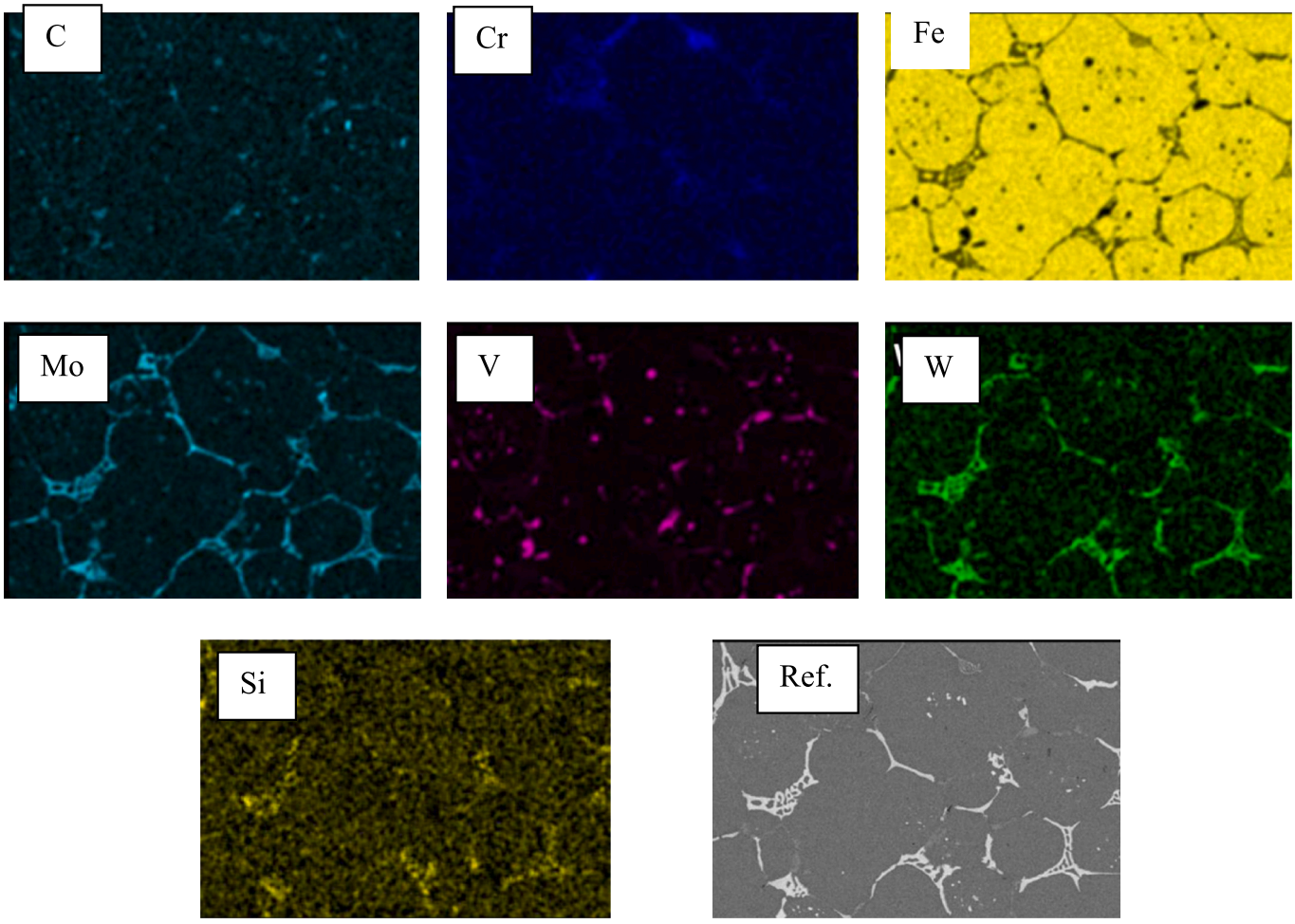

Fig. 21. EDS-SEM mapping in the sample sintered with a dwell time of 2 h, by EDX.

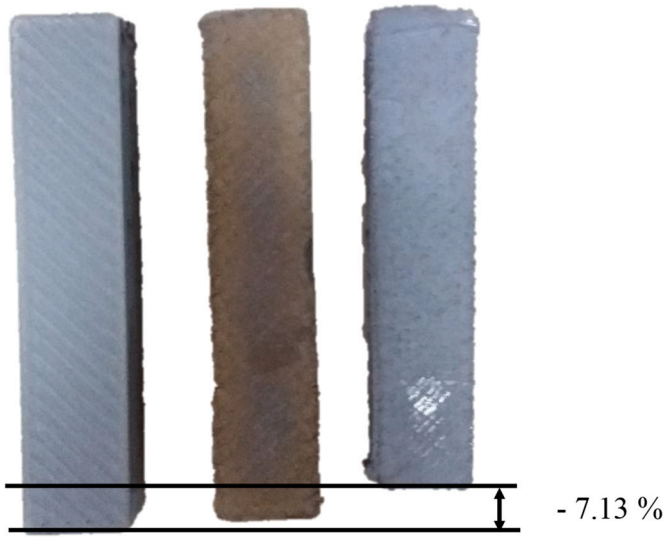

Fig. 22. Shrinkage as a function of manufacturing steps, from 3D printing to final sintering for a thick prismatic component.

gas emission of the printed sample in terms of spectral absorbance, and in dotted line the absorbance for the binder only. The absorbance has no unity, and comparisons are pertinent only if they are done on a single test. While the emissions of CO and CO_2 are similar, with just a lower intensity between the printed sample and the reference one, the $C_xH_yO_z$ components in the sample present a dramatic increase in intensity in absorbance between 200 and 700 °C. This increase can be explained by either a chemical reaction between the polymer and the powder, or a modification of the powder's chemical composition during the printing stage. This latter hypothesis is corroborated as the printing stage is conducted at a temperature higher than 190 °C, where the TGA graph (Fig. 13) reveals the beginning of the material degradation.

The thermogravimetric analysis of a debinded sample in Fig. 15 shows that mass difference is anecdotal after the debinding cycle; a gain of 0.03%w proves that the debinding cycle has fully degraded the polymer.

Table 11 illustrates the evolution of the porosity for the debinding step according to a starting porosity. After debinding, the measured porosity does not include the porosity between the powder grains, which are too small to be measured by tomography. Only the macro-porosity is evaluated as only pores >5 μm^3 can be measured. A minimal porosity after printing is not the optimal parameter to ensure a minimal porosity after debinding, instead a controlled porosity allows the degraded polymer gas to escape without creating macro-pores or without delaminating the part.

Fig. 16 represents the 3D reconstruction of the debinded part thanks to the RX tomography. The part volume is in light grey where coloured spots represent the pores; the different colours correspond to the different volume sizes of pores. In Fig. 16 a), where a weak porosity exists in the printed part, the pores create a vertical dotted line, corresponding to the start point of the printing trajectory. Effectively, half of the layers starts the deposition on the left of this line, the other half of

layers is oriented at 90° of the first line. The beginning of the printing trajectory does not cover its ending point, leading to the creation of a discontinuous vertical line of pores as represented in Fig. 16 a). After debinding (Fig. 16 b)), the part is dotted with pores created by the degradation phenomenon, where the gases move away the molten binder and powder grains generating bubbles. The exterior pores (in deep blue and green) are located between seams of the outline paths, and the internal pores (in light blue) are randomly located.

In Fig. 16 c), vertical lines of pores can also be observed, where the additional vertical line corresponds to the filling printing trajectory. The print strategy is also visible, as space in between seams is not totally covered by the print. This creates a network of pores, which forms almost a continuous network of all the porosity in the form of horizontal lines. This network allows the gas created during binder degradation to escape, even if it's at the heart of the part, thus preventing bubbles or delamination. After debinding, the network is still visible, but no additional pores have been created, as shown in Fig. 16 d).

3.6. Densification

Dilatometry is selected to determine the best sintering temperature as described in part 1.6. The resulting dilatometry analysis is illustrated in Fig. 17 where the range of the sintering temperature is defined by the domain where the derivative of the height curve is negative. This shrinkage curve can be divided into four domains in which different phenomena take place. If the domains 1 and 2 are associated to the thermal expansion of powders and the granular rearrangement respectively, the domain 3 consists of the sintering at the solid state whereas the domain 4 is led to the presence of liquid phase before the melting of steel. Consequently, the sintering temperature will be chosen between 1100 °C and 1260 °C. Indeed, at 1225 °C, the sintering rate increases significantly meaning that sintering at the solid state is taking place. For temperatures higher than 1260 °C, the sintering rate becomes irregular caused by the local melting phenomena (such as eutectic, transus, …).

Finally, a natural sintering at 1250 °C during 2 h follows by a cooling down with a rate of 50 °C/min is selected. Nevertheless, to limit all overshoot, two heating rates were applied, one at 50 °C/min up to 1150 °C then a second at 25 °C/min to 1250 °C.

Various samples, starting from each granulometry class, have been sintered according to this thermal cycle to produce the parts shown in Fig. 18. These three samples are representative and have been chosen randomly. They present some small differences. On the 0–45 μm sample (Fig. 19 a)), the print layers are quite invisible, whereas they are distinguishable on the 0–63 μm (Fig. 19 b)) and 0–106 μm samples (Fig. 19 c)). As all the samples have undergone the same sintering process, and as only their specific surface parameters are different, it can be concluded that these differences are due to the particle powder size. With a larger specific surface, the smaller powder presents a larger area for interaction and thus leads to a better sintering [54].

When the densification step takes place at a temperature higher than 1250 °C, regardless of the temperature holding time, geometric defects appear. Table 12 presents the results of the sintering in terms of porosity and height variation for a sintering at 1250 °C during 2 h, respectively for the 0–45 μm, 0–63 μm and 0–106 μm powders.

The tomography presented in Fig. 19 is relative to the powder 0–63 μm, it shows that the porosity evolves during the densification stage; the micropores created between the powder particles during debinding stage merge to form the larger pores. Consequently, porosity increases from 0.52% to 0.97% during that step (with a ± 1% uncertainty).

The sintering of the printed/debinded specimens depend largely on the size of initial particle powders. Indeed, a small powder granulometry presents a better “sinterability”, and thus produces a lower internal porosity. The powder 0–45 μm was selected for further studies, as it is the only powder capable of producing a final porosity inferior to 3%. For this reason, only the sintered specimen with a porosity inferior to 3%, prepared from 0 to 45 μm powders will be discussed below.

Firstly, the surface quality was evaluated by a measurement of the arithmetic roughness *Ra*. Usually, dwell time during the sintering step is critical to optimize the microstructure and the surface roughness. A higher dwell time creates a smoother surface, as the metallic grains reorganize and optimize the surface tension. An increase of dwell time leads to a smoother surface that overturn the initial high roughness and a larger surface layer. A *Ra* of 18 μm can be obtained with a dwell time equal to 2 h.

Secondly, sintered parts are sliced and polished to observe their microstructure using SEM-FEG microscope. The Fig. 20 shows that it exists a microstructure gradient between the surface and the centre of the part. Indeed, a surface structure of 500 μm depth is observed. An increase in dwell time is correlated with an increase in the thickness of this surface layer. In this figure, a coarse microstructure and some larger pores (size close 10 to 30 μm, in dark due to the presence of resin) are observed at the surface. The surface structure can be explained by a difference in terms of temperature between the surface and the inside of the part. With a long dwell time, the gradient is lowered, and the affected area is larger, and with a longer dwell time, the metal grains have more time to reorganize.

On this figure, the backscattered electrons give different information on the chemical composition, as the grey level difference is caused by the atomic weight of each element. The heavier elements of the steel alloy are grouped in the whiter grains (Mo and W) and create eutectic structure, which separate the darker zones containing Fe. Other grey grains contain a majority of the other elements (Cr, C and V), and a minority of Mo. A better description of this chemical repartition is given on the Fig. 21 where EDS-SEM mappings are presented for each major element constituting this alloy.

This segregation of the addition elements is explained by the fact that a liquid phase of the surface layer takes place. Some elements as iron melt due to a higher temperature allowing a dissolution of others elements and solidify during the cooling. Indeed, the difference in terms of solubility between the solid and liquid phases allows to concentrate heavy elements into the eutectic [55] and, thus to create grains composed of W, Mo and Si [56]. In addition, other elements as Cr and V, in presence of carbon, leads to the formation of carbides.

Finally, the microstructure of these specimens is in line with what is observed in the literature. However, to obtain fully dense parts, the alternative solution is to combine our printing technique with hot pressing such as SPS or HIP.

3.7. Shrinkage and mechanical properties

The influence of powder particle size in terms of final porosity and shrinkage is compared with the Table 12. The 0–45 μm powder filler can be sintered to a porosity of <3%, while the other fillers cannot be sintered to a porosity of <4%, and the shrinkage is around 13.35%. This particle size could be further reduced to a conventional PIM process particle size with an average diameter of 16 to 22 μm.

To illustrate the use of optimum printing parameters, as well as optimal debinding and densification kinetics for the finest particle size powder (0–45 μm), a thick prismatic component has been printed. Observation of the printed, debinded and sintered prism illustrates the geometric and surface quality obtained after the FGF process and the debinding and sintering steps, see Fig. 22. The evolution of shrinkage as a function of manufacturing stages, from 3D printing to final sintering, is also illustrated on the same figure.

4. Conclusion

This work shows that a bio-based binder is suitable for MEX process. The binder is a simple mix of Polylactic Acid and Stearic Acid, a backbone plus a surfactant. It is debinded within a single thermal step. It allows a quick debinding cycle compared to most of the solvent plus thermal debinding binders.

The binder was mixed with an ASP2023 steel tool alloy powder with three different granulometries. The resulting feedstocks are loaded up to 68%vol. with powder. They have been fully measured and modelled, and proved to be homogeneous and printable. The powder granulometry has an influence on the rheology, especially when changing from a 0–45 μm powder to another. The 0–63 μm and 0–106 μm powders present no significant differences. The surfactant proportion is set at 0.48% wt. of the feedstock in the formulation of the optimised binder, i.e. a concentration varying from 105 to 162 $mg{\cdot}m^{-2}$ for the powder. This surfactant concentration is considerable comparatively to the literature, and its variation should not affect the feedstock viscosity.

The print stage proves to be crucial. A low controlled porosity is favourable to a thermal degradation. By opposition, a fully dense printed part results in delamination and pores creation during the sintering stage.

The density can reach up to 97.45% with a conventional sintering process, leading to functional parts. They can undergo further sintering to lower the porosity if necessary. The proposed sintering process produces a significantly denser part when using the 0–45 μm powder compared to the other two powders. However, obtaining a dense material with a controlled microstructure will require mastering all the mechanisms associated with the printing and debinding stages in order to better control the natural sintering stage and, thus, consider a densification stage by HIP (Hot Isostatic Pressing) coupled with the conduct of heat treatments to achieve improved mechanical properties.

CRediT authorship contribution statement

N. Charpentier: Writing – original draft, Methodology, Investigation. **T. Barrière:** Writing – review & editing, Supervision, Funding acquisition, Conceptualization. **F. Bernard:** Writing – review & editing, Supervision, Conceptualization. **N. Boudeau:** Writing – review & editing, Supervision, Methodology, Investigation. **A. Gilbin:** Validation, Methodology, Investigation, Conceptualization. **P. Vikner:** Writing – review & editing, Validation, Resources, Conceptualization.

Declaration of competing interest

The authors declare that they have no known competing financial interests or personal relationships that could have appeared to influence the work reported in this paper.

Data availability

Data will be made available on request.

Acknowledgement

The authors thank the EIPHI Graduate School which has supported this work under the contract NR-17-EURE-0002. They also thank the MIFYSTO and MIMENTO technical centres for their assistance and expertise, respectively for the SEM and tomographic analysis.

References

[1] M. Allahverdi, S.C. Danforth, M.A. Jafari, A. Safari, Processing of advanced electroceramic components by fused deposition technique, J. Eur. Ceram. Soc. 21 (2001) 110–111.
[2] R.M. German, Injection Molding of Metals and Ceramics, in: Powder Metallurgy, Metal Powder Industries Federation, Princetion, 1997.
[3] A. Dehghan-Manshadi, P. Yu, M. Dargush, D. StJohn, M. Qian, Metal injection moulding of surgical tools, biomaterials and medical devices: a review, Powder Technol. 1364 (2020) 189–204, https://doi.org/10.1016/j.powtec.2020.01.073.
[4] S.I. Roshchupkin, V.I. Golovin, A.G. Kolesov, A.Y. Tarakhovskiy, Extruder for the production of metal-polymer filament for additive technologies, IOP Conf. Ser.: Mater. Sci. Eng. 971 (2020) 022009, https://doi.org/10.1088/1757-899X/971/2/022009.
[5] C. Suwanpreecha, A. Manonukul, A review on material extrusion additive manufacturing of metal and how it compares with metal injection moulding, Metals 12 (2022) 429, https://doi.org/10.3390/met12030429.
[6] J.-C. Wang, H. Dommati, S.-J. Hsieh, Review of additive manufacturing methods for high-performance ceramic materials, Int. J. Adv. Manuf. Technol. 103 (2019) 2627–2647, https://doi.org/10.1016/j.powtec.2020.01.073.
[7] E. Peng, D. Zhang, J. Ding, Ceramic robocasting: recent achievements, potential, and future developments, Adv. Mater. 30 (2018), https://doi.org/10.1002/adma.201802404.
[8] C.B. Williams, J.K. Cochran, D.W. Rosen, Additive manufacturing of metallic cellular materials via three-dimensional printing, Int. J. Adv. Manuf. Technol. 53 (2011) 231–239, https://doi.org/10.1007/s00170-010-2812-2.
[9] K. Rane, M. Strano, A comprehensive review of extrusion-based additive manufacturing processes for rapid production of metallic and ceramic parts, Adv. Manuf. 7 (2019) 155–173, https://doi.org/10.1007/s40436-019-00253-6.
[10] H. Ramazani, A. Kami, Metal FDM, a new extrusion-based additive manufacturing technology for manufacturing of metallic parts: a review, Prog. Addit. Manuf. 7 (2022) 609–626, https://doi.org/10.1007/s40964-021-00250-x.
[11] J. Gonzalez-Gutierrez, S. Cano, S. Schuschnigg, C. Kukla, J. Saptoka, C. Holzer, Additive manufacturing of metallic and ceramic components by the material extrusion of highly-filled polymers: a review and future perspectives, Materials 11 (2018) 1840, https://doi.org/10.3390/ma11050840.
[12] J. Vetter, F. Huber, S. Wachter, C. Körner, M. Schmidt, Development of a material extrusion additive manufacturing process of 1.2083 steel comprising FFF printing, solvent and thermal debinding and sintering, Procedia CIRP 113 (2022) 341–346, https://doi.org/10.1016/j.procir.2022.09.140.
[13] Z. Lu, O.I. Ayeni, X. Yang, H.-Y. Park, Y.-G. Jung, J. Zhang, Microstructure and phase analysis of 3D-printed components using bronze metal filament, J. Mater. Eng. Perform. 29 (2020) 1650–1656, https://doi.org/10.1007/s11665-020-04697-x.
[14] W. Lengauer, I. Duretek, M. Fürst, V. Schwarz, J. Gonzalez-Gutierrez, S. Schuschnigg, C. Kukla, M. Kitzmantel, E. Neubaeur, C. Lieberwirth, V. Morrison, Fabrication and properties of extrusion-based 3D-printed hardmetal and cermet components, Int. J. Refract. Met. Hard Mater. 82 (2019) 141–149, https://doi.org/10.1016/j.ijrmhm.2019.04.011.
[15] G. Singh, J.-M. Missiaen, D. Bouvard, J.-M. Chaix, Additive manufacturing of 17–4 PH steel using metal injection molding feedstock: analysis of 3D extrusion printing, debinding and sintering, Addit. Manuf. 47 (2021), https://doi.org/10.1016/j.addma.2021.102287.
[16] V. Siracusa, I. Blanci, Bio-polyethylene (Bio-PE), bio-polypropylene (bio-PP) and bio-poly(ethylene terephthalate) (bio-PET): recent developments in bio-based polymers analogous to petroleum-derived ones for packaging and engineering applications, Polymers 12 (18) (2020), https://doi.org/10.3390/polym12081641.
[17] A. Royer, T. Barrière, J.-C. Gelin, L. Hilliou, Development and characterisation of a biosourced feedstock of superalloy in metal injection moulding process, Powder Metall. 60 (12) (2017) 105–111, https://doi.org/10.1080/00325899.2016.1269457.
[18] N. Toropkov, M. Lerner, E. Mironov, Feedstock investigation based on SAE 316L steel bimodal powders and PLA/PMMA for injection molding: an experimental study, AIP Conf. Proc. 2167 (11) (2019) 020367, https://doi.org/10.1063/1.5132234.
[19] F. Clemens, F. Sarraf, A. Borzì, A. Neels, A. Hadian, Material extrusion additive manufacturing of advanced ceramics: towards the production of large components, J. Eur. Ceram. Soc. 43 (2023) 2752–2760, https://doi.org/10.1016/j.jeurceramsoc.2022.10.019.
[20] R. Wick-Joliat, M. Schroffenegger, D. Penner, Multi-material ceramic material extrusion 3D printing with granulated injection molding feedstocks, Ceram. Int. 49 (2023) 6361–6367, https://doi.org/10.1016/j.ceramint.2022.10.170.
[21] C. Lieberwirth, A. Harder, H. Seitz, Extrusion based additive manufacturing of metal parts, J. Mech. Eng. Automat. 7 (2017), https://doi.org/10.17265/2159-5275/2017.02.004.
[22] G. Singh, J.-M. Missiaen, D. Bouvard, J.-M. Chaix, Copper additive manufacturing using MIM feedstock: adjustment of printing, debinding, and sintering parameters for processing dense and defectless parts, Int. J. Adv. Manuf. Technol. 115 (2021) 449–462, https://doi.org/10.1007/s00170-021-07188-y.
[23] G. Singh, J.-M. Missiaen, D. Bouvard, J.-M. Chaix, Copper extrusion 3D printing using metal injection moulding feedstock: analysis of process parameters for green density and surface roughness optimization, Addit. Manuf. 38 (2021) 101778, https://doi.org/10.1016/j.addma.2020.101778.
[24] K. Kassym, A. Perveen, Atomization processes of metal powders for 3D printing, Mater. Today Proc. 26 (2020) 1727–1733, https://doi.org/10.1016/j.matpr.2020.02.364.
[25] S.J. Rohenberg, D.K. Flynn, A.F. Eidson, J.A. Mewhinney, G.J. Newton, Determination of specific surface area by krypton adsorption, comparison of three different methods of determining surface area, and evaluation of different specific surface area standards, J. Colloid Interface Sci. 116 (12) (1987) 541–554, https://doi.org/10.1016/0021-9797(87)90150-0.
[26] X. Kong, C. Quinard, T. Barrière, J.-C. Gelin, Mixing and characterisation of stainless steel 316L feedstock, Int. J. Mater. Form. 2 (2009) 1709, https://doi.org/10.1007/s12289-009-0652-0.
[27] F.M. Barreiros, A.G. Martins, M. Matos, J. Mascarenhas, M.T. Vieira, Preparing MIM feedstocks for bio-applications using an agar-based binder, Mater. Sci. Forum 587-588 (2008) 385–389, https://doi.org/10.4028/www.scientific.net/MSF.587-588.385.
[28] X. Kong, T. Barriere, J.C. Gelin, Determination of critical and optimal powder loadings for 316L fine stainless steel feedstocks for micro-powder injection

molding, J. Mater. Process. Technol. 212 (2012) 2173–2182, https://doi.org/10.1016/j.jmatprotec.2012.05.023.
[29] J.D. Ferry, Viscoelastic Properties of Polymers, John Wiley & Sons, 1980.
[30] M. Strano, K. Rane, F. Briatico Vangosa, L. Di Landro, Extrusion of metal powder-polymer mixtures: melt rheology and process stability, J. Mater. Process. Technol. 273 (2019) 116250, https://doi.org/10.1016/j.jmatprotec.2019.116250.
[31] S.B. Balani, F. Chabert, V. Nassiet, A. Cantarel, Influence of printing parameters on the stability of deposited beads in fused filament fabrication of poly(lactic) acid, Addit. Manuf. 25 (2019) 112–121, https://doi.org/10.1016/j.addma.2018.10.012.
[32] R.M. German, Sintering Theory and Practice, Wiley-Interscience, 1996.
[33] K. Benié, T. Barrière, V. Placet, A. Cherouat, Introducing a new optimization parameter based on diffusion, coalescence and crystallization to maximize the tensile properties of additive manufacturing parts, Addit. Manuf. 69 (2023) 103538, https://doi.org/10.1016/j.addma.2023.103538.
[34] K.D. N'dri, N. Charpentier, L. Hirsinger, A. Gilbin, T. Barriere, Highly loaded magnetocaloric composites by La(Fe,Si)13H powder dedicated to extrusion-based additive manufacturing applications, Powder Technol. 425 (2023) 118616, https://doi.org/10.1016/j.powtec.2023.118616.
[35] T. Hanmann, R. Heldele, Fatty acid surfactant structure–feedstock flow properties: correlation for high-pressure ceramic injection molding, Int. J. Appl. Ceram. Technol. 8 (16) (2011) 1296–1304, https://doi.org/10.1111/j.1744-7402.2011.02612.x.
[36] J. Bricout, J.-C. Gelin, C. Ablitzer, P. Matheron, M. Brothier, Influence of powder characteristics on the behaviour of PIM feedstock, Chem. Eng. Res. Des. 91 (2013) 112, https://doi.org/10.1016/j.cherd.2013.02.023.
[37] Y.M. Li, W.Q. Liu, F.H. Luo, J.L. Yue, Effects of surfactant on properties of MIM feedstock, Trans. Nonferrous Metals Soc. China 17 (11) (2007) 1–8, https://doi.org/10.1016/S1003-6326(07)60039-9.
[38] M.C. Auscher, R. Fulchiron, N. Fougerouse, T. Périé, P. Cassagnau, Zirconia based feedstocks: influence of particle surface modification on the rheological properties, Ceram. Int. 43 (2017) 118, https://doi.org/10.1016/j.ceramint.2017.09.100.
[39] P. Czyzewski, D. Marciniak, B. Nowinka, M. Borowiak, M. Bielinski, Influence of extruder's nozzle diameter on the improvement of functional properties of 3D-printed PLA products, Polymers 14 (2022) 1356, https://doi.org/10.3390/polym14020356.
[40] M. Spoerk, J. Gonzalez-Gutierrez, J. Sapkota, S. Schuschnigg, C. Holzer, Effect of the printing bed temperature on the adhesion of parts produced by fused filament fabrication, Plast. Rubber Compos. 47 (11) (2018) 17–24, https://doi.org/10.1080/14658011.2017.1399531.
[41] S. Rolere, U. Soupremanien, M. Bohnke, M. Dalmasso, C. Delafosse, R. Laucournet, New insights on the porous network created during solvent debinding of powder injection-molded (PIM) parts, and its influence on the thermal debinding efficiency, J. Mater. Process. Technol. 295 (2021) 117163, https://doi.org/10.1016/j.jmatprotec.2021.117163.
[42] T.-Y. Chan, S.-T. Lin, Effects of stearic acid on the injection molding of alumina, J. Am. Ceram. Soc. 78 (1995) 110, https://doi.org/10.1111/j.1151-2916.1995.tb08050.x.
[43] V. Momeni, A. Askari, M.H. Alaei, A.H. Rahimi, K. Nekouee, H. Zangi, The effect of powder loading and binder system on the mechanical, rheological and microstructural properties of 4605 powder in MIM process, Trans. Indian Inst. Metals 72 (2019) 1245–1254, https://doi.org/10.1007/s12666-019-01615-1.
[44] M. Trunec, J. Cihlář, Thermal removal of multicomponent binder from ceramic injection mouldings, J. Eur. Ceram. Soc. 22 (2002) 113, https://doi.org/10.1016/S0955-2219(02)00015-8.
[45] J. Wen, Z. Xie, W. Cao, X. Yang, Effects of different backbone binders on the characteristics of zirconia parts using wax-based binder system via ceramic injection molding, J. Adv. Ceram. 5 (2016) 321–328, https://doi.org/10.1007/s40145-016-0205-1.
[46] P. Thomas-Vielma, A. Cervera, B. Levenfeld, A. Vàrez, Production of alumina parts by powder injection molding with a binder system based on high density polyethylene, J. Eur. Ceram. Soc. 28 (14) (2008) 763–771, https://doi.org/10.1016/j.jeurceramsoc.2007.08.004.
[47] S.M. Ani, A. Muchtar, N. Muhamad, J.A. Ghani, Binder removal via a two-stage debinding process for ceramic injection molding parts, Ceram. Int. 40 (12) (2014) 2819–2824, https://doi.org/10.1016/j.ceramint.2013.10.032.
[48] L.U. Lopes, M.A. Carvalho, R.S. Chaves, M.P. Trevisan, P.A. Wendhausen, H. Takiishi, Study of carbon influence on magnetic properties of metal injection molding Nd-Fe-B based magnets, Mater. Sci. Forum 1 (2012) 2727–2728, https://doi.org/10.4028/www.scientific.net/MSF.727-728.124.
[49] L.U. Lopes, T. Hartwig, P.A. Wenshausen, Evaluation of process variables in the alignment factor of Nd-Fe-B magnets made by metal injection molding, IEEE Trans. Magn. 49 (18) (2013) 4618–4621, https://doi.org/10.1109/TMAG.2013.2259802.
[50] L.U. Lopes, P.V. Souza Lia Fook, A. Owczarzak, N. Uenal, T. Hartwig, P. A. Wendhausen, Feasibility study for feedstock recycling on PIM Nd-Fe-B permanent magnets, Mater. Sci. Forum 802 (2014) 574–578, https://doi.org/10.4028/www.scientific.net/MSF.802.574.
[51] A. Royer, T. Barrière, Y. Bienvenu, Influence of supercritical debinding and processing parameters on final properties of injection-moulded Inconel 718, Powder Technol. 336 (2018) 311–317, https://doi.org/10.1016/j.powtec.2018.05.047.
[52] E. Hnatkova, B. Hausnerova, A. Hales, L. Jiranek, F. Derguti, I. Todd, Processing of MIM feedstocks based on Inconel 718 powder and partially water-soluble binder varying in PEG molecular weight, Powder Technol. 322 (2017) 439–446, https://doi.org/10.1016/j.powtec.2017.09.029.
[53] M.D. Hayat, P.P. Jadhav, H. Zhang, S. Ray, P. Cao, Improving titanium injection moulding feedstock based on PEG/PPC based binder system, Powder Technol. 330 (2018) 304–309, https://doi.org/10.1016/j.powtec.2018.02.043.
[54] M. Moghadasi, W. Du, M. Li, Z. Pei, C. Ma, Ceramic binder jetting additive manufacturing: effects of particle size on feedstock powder and final part properties, Ceram. Int. 46 (2020) 16966–19672, https://doi.org/10.1016/j.ceramint.2020.03.280.
[55] V.P. Titov, The solubility of tungsten in molten iron, Powder Metall. Met. Ceram. 32 (1994) 911–912, https://doi.org/10.1007/BF00559647.
[56] G.V. Raynor, V.G. Rivlin, 5: critical evaluation of constitutions of certain ternary alloys containing iron, tungsten, and a third metal, Int. Metals Rev. 26 (1981) 213–249, https://doi.org/10.1179/imtr.1981.26.1.213.